



MONASH University

**Investigation on the Effects and Performance of
Underwater Imaging Target Detection**

Yam Jian Wei

Master of Engineering Science (Research)

A thesis submitted for the degree of Master at

Monash University in 2021

Malaysia School of Engineering

Copyright notice

© Yam Jian Wei (2021).

Abstract

Various factors in underwater imaging are investigated in this study, including the effect of water turbulence, salinity, and turbidity. The experimental results are analyzed based on reflection ratio and range error accuracy. The experimental results show that the reflection ratio has an inversely proportional trend with water turbulence, salinity, and turbidity effects. Among the three factors, the reflection ratio of reflected intensity shows the most considerable reduction in the water turbidity effect. Moreover, the range error shows consistent and no significant variations with the increase of water turbulence and salinity. However, the range error shows an obvious decreasing trend with higher water turbidity. This is mainly due to the significant absorption effect in higher water turbidity levels compared to other factors. This shows that the reflected power decreases. Thus, the effect of water turbidity and wavelength of laser source are further studied in underwater single-pixel imaging (SPI) system which uses a pulse laser as a light source. The results have shown that using a longer wavelength laser source helps to reduce the scattering effect and improve the overall image reconstruction performance. In this study, the block compressive sensing technique is applied in underwater SPI, and results have shown that reconstruction performance is convincing even at a low sampling rate. The presented findings build a comprehensive understanding of target reflection with the influence of medium effect for the underwater object detection system. This study provides a reference for future improvement on the underwater laser sensing system and imaging system.

Declaration of Originality

This thesis is an original work of my research and contains no material which has been accepted for the award of any other degree or diploma at any university or equivalent institution and that, to the best of my knowledge and belief, this thesis contains no material previously published or written by another person, except where due reference is made in the text of the thesis.

Signature:

Print Name:Yam Jian Wei....

Date:12/3/2021.....

Publications

Journal Paper

1. M. Li, A. Mathai, S. L. H. Lau, J. W. Yam, X. Xu, and X. Wang, "Underwater Object Detection and Reconstruction Based on Active Single-Pixel Imaging and Super-Resolution Convolutional Neural Network," *Sensors (Basel)*, vol. 21, no. 1, p. 313, 2021, doi: 10.3390/s21010313.
2. Q. Chen, J. W. Yam, S. Y. Chua, N. Guo, and X. Wang, "Characterizing the performance impacts of target surface on underwater pulse laser ranging system," *Journal of quantitative spectroscopy & radiative transfer*, vol. 255, p. 107267, 2020, doi: 10.1016/j.jqsrt.2020.107267.

Conference Presentation

ISALSars'19, The 6th International Symposium on Atmospheric Light Scattering and Remote Sensing.

Presentation title: Investigation of Water Turbulence and Salinity on Underwater Pulse Laser Ranging System

Acknowledgment

Completing a postgraduate study is a challenging but excellent job throughout my academic study. The preparation of this thesis would not be possible without the valuable guidance and help from many people, and I would like to take this opportunity to thank them.

Firstly, I would like to thank my supervisors Associate Professor Wang Xin and Professor Anthony Guo, for their continuous support. I sincerely thank them for their valuable guidance and advice.

I am also very much grateful for the financial support and funding from Monash University Malaysia.

I would also take this chance to express my gratitude to Mr. Eddy Chow Mun Tik, Ms. Anumol Mathai, Ms. Li Meng Di, Ms. Chua Sing Yee, and Mr. Stephen Lau Lee Huei for their friendly advice and co-operation throughout my study period.

Finally, it is my privilege to thank my family, who have inspired me to pursue postgraduate study. I sincerely thank them for always staying with me to encourage and support me throughout my entire life. Without them, I might not be able to finish this thesis.

Contents

Abstract	iii
Publications	v
Acknowledgment	vi
Contents	vii
List of Figures	ix
List of Tables	x
Chapter 1 Introduction	1
1.1 Background	1
1.2 Research Motivations	4
1.3 Research Objectives	4
1.4 Organization of Thesis	5
Chapter 2 Literature Review	6
2.1 Influence Factors and Considerations of Underwater Laser Sensing System.....	6
2.1.1 Laser Source and Profile.....	6
2.1.2 Atmospheric Effects	7
2.2 Underwater Imaging.....	12
2.2.1 Overview of Imaging System	12
2.2.2 Underwater Imaging System	16
2.3 Single-pixel Imaging	17
2.3.1 Overview of Single-pixel Imaging	17
2.3.2 Applications.....	21
Chapter 3 Medium Effect on Underwater Light Propagation.....	24
3.1 Experimental Setup	24
3.2 Experimental Procedures.....	26
3.2.1 Data Collection	26
3.2.2 Reflection ratio	27
3.2.3 Range Determination	28
3.3 Results and Discussion.....	30
3.3.1 Water Turbulence Effect	30
3.3.2 Water Salinity Effect	33
3.3.3 Water Turbidity Effect.....	37

3.3.4 Summary.....	40
Chapter 4 Underwater Single-Pixel Imaging Quality.....	41
4.1 Underwater Single-Pixel Imaging System Setup.....	41
4.2 Single-Pixel Imaging Reconstruction via Block Compressive Sensing	43
4.2.1 Compressive Sensing.....	43
4.2.2.1 Conventional Compressive Sensing	43
4.2.2.2 Block Compressive Sensing	45
4.2.2 Image Reconstruction Algorithm via Block Compressive Sensing	46
4.3 Underwater Single-Pixel Imaging Quality Evaluation.....	48
4.4 Results and Discussion.....	49
4.4.1 The Effect of Image Resolution and Number of Measurements	49
4.4.2 The Effect of Water Turbidity Level.....	53
4.4.3 The Effect of Laser Source Wavelength.....	56
Chapter 5 Conclusion.....	60
5.1 Summary of Findings	60
5.2 Future Work	62
References.....	63

List of Figures

Figure 1 Column and row major ordering	17
Figure 2 Schematic diagram of underwater laser ranging system experimental setup.....	25
Figure 3 Experimental setup of underwater pulse ranging system.....	25
Figure 4 The electrical signals detected from the oscilloscope. The electrical signal is shown in purple color representing the laser source signal, while the electrical signal in blue color representing the reflection detected after hitting the target.	27
Figure 5 The range error obtained experimentally against different water turbulence strength (L/min).....	30
Figure 6 The reflection ratio obtained experimentally against different water turbulence strength	32
Figure 7 The range error obtained experimentally against different water salinity concentration(g/ml).....	33
Figure 8 The reflection ratio obtained experimentally against different water salinity concentration (g/ml).....	34
Figure 9 Zhang et al. has compared the experimental result with the proposed theoretical model (equation 14) [93]	35
Figure 10 The range error obtained experimentally against different water turbidity level (NTU)	37
Figure 11 The reflection ratio obtained experimentally against different water turbidity level (NTU)	39
Figure 12 Schematic diagram of underwater single-pixel imaging.....	42
Figure 13 Experimental setup of underwater single-pixel imaging.....	42
Figure 14 Flowchart of the single-pixel imaging reconstruction algorithm.	47
Figure 15 Reconstructed images with the same number of total measurements, 64 measurements.	49
Figure 16 Reconstructed images with a different number of measurements and same resolution level.....	50
Figure 17 PSNR/dB against the number of measurements of reconstructed images	52
Figure 18 SSIM against the number of measurements of reconstructed images.....	52
Figure 19 Reconstructed images on different water turbidity level with the same number of measurements and image resolution	53
Figure 20 PSNR/dB against turbidity level (NTU) with the same number of measurements.....	55
Figure 21 SSIM against water turbidity level (NTU) with the same number of measurements. .	55
Figure 22 Reconstructed images with different water turbidity levels in red laser source.....	56
Figure 23 Reconstructed images with different water turbidity levels by comparison in red and green laser source.....	57
Figure 24 PSNR/dB against turbidity level (NTU) by comparison in red and green laser source.	59
Figure 25 SSIM against turbidity level (NTU) by comparison in red and green laser source.	59

List of Tables

Table 1 Summary of advantages and drawbacks for the conventional imaging system.	15
Table 2 Summary of advantages and drawbacks of the modulation method of single-pixel imaging.	20

Chapter 1 Introduction

1.1 Background

Laser sensing has been a popular research field in machine vision and object detection due to its noncontact and nondestructive nature [1-3]. It has applications in various fields, including object recognition, modeling, surface scanning and profiling, and 3D Vision [4-7]. In the laser sensing system, the laser beam illuminates the target surface, and the light backscattering signal is generated. The backscattering signal received by the sensors carries essential information on range detection. The laser emitted will change direction and attenuates along with the laser propagation and reflection after hitting the target. Hence, many factors contribute to the changes in the reflected signals received, and the system accuracy and performance rely heavily on these factors, including the laser, target, sensor, and medium [8, 9].

Underwater laser sensing is a more complicated laser detection process as the underwater environment varies not only in light transmittance medium but also in the optical characteristics. The underwater medium contributes more loss of attenuation energy than the air medium due to different coefficients of light absorption and scattering. The water medium is also causing more noises in the reflected laser signal. In general, the light beam transmission and attenuation underwater by 1 meter is equivalent to the light transmission in the air by approximately 800 meters [10]. This is caused by many factors, such as water density, temperature, and disturbance. These factors will lead to a change in the refractive index and scattering effect and eventually cause wavefront distortion and a decrease in system resolution [11]. Thus, this limits the application of the laser sensing system in an underwater environment. Therefore, this is important to understand the factors of the underwater laser sensing system to improve system performance.

Many factors could cause changes in underwater light beam transmission and attenuation, such as laser source, target material, incident angle, water temperature, density, turbidity, turbulence, and salinity. In this study, the effect of a laser source, water turbulence, salinity concentration, and turbidity in the medium will be investigated. Underwater turbulence has a significant impact on momentum, heat, and water diffusion. These factors contribute to variations in the reflected laser signal [12, 13]. Therefore, the understanding of the effect of water turbulence in underwater light beam transmission is essential as underwater applications usually involve turbulent flow. Secondly, the impact of water salinity on underwater target detection is also necessary to be studied as the application in seawater is increasing. The salinity of seawater is different from regions, and therefore the underwater refractive index would be different as well. Moreover, the turbidity of the underwater medium will cause variation in laser propagation. The turbidity level leads to the variation of absorption and backscattering of the propagation medium and eventually affects the reflectance of the illuminated source. Thus, the understanding of the relationship between turbidity level of underwater medium and the reflectance will help to improve the system performance.

The effect of these factors could eventually cause variations to the reflections of the laser source. The reflection has been widely studied due to the high interest in underwater imaging. There are various applications of an underwater imaging system such as benthic surveys, an inspection of oil and gas underwater infrastructure. One of the most widely used underwater imaging systems with extended range is the serial laser line scan (LLS) system. LLS system is the system where the illuminator and receiver are on the same platform. LLS system consists of scanning electronics, mechanical, and optics components to ensure both the illuminator and receiver scan the target region by a line synchronously. The sensor completes the entire image

with the forward motion of the platform [14]. However, the imaging speed of the LLS system is considered slow as it requires scanning line-by-line. Thus, another attempt, single-pixel imaging with compressive sensing in the underwater environment, is studied [15]. Single-pixel imaging with compressive sensing offers the potential to reduce the compactness, complexity, and system cost by reducing the camera to one unit instead of using many sensors in the detector array. Compressive sensing also helps to reduce the time required for image acquisition due to sampling at the Nyquist rate. This eventually helps to reduce reconstruction computational time due to lesser data. Thus, the main advantage of this technique is the ability to recover multi-pixel images at a faster speed compared with the conventional scanning methods.

Therefore, it is necessary to study these factors to improve the performance of the system. The accuracy and quality of the underwater imaging system could help to improve the performance of the applications.

1.2 Research Motivations

As underwater sensing application has been increasing in the real world, many researches on underwater sensing have been carried out in recent years to improve the system performance. However, underwater sensing application has various limitations and difficulties such as system stability, consistency, and high cost etc. The investigation on the influence factors in an underwater medium is essential to improve the performance of underwater laser sensing. In this study, various factors in underwater imaging are investigated, including the effect of water turbulence, salinity, and turbidity. Furthermore, different factors affecting underwater single-pixel imaging quality are investigated. The findings of this study will build a comprehensive understanding of target reflection with the influence of medium effect for the underwater object detection system, and provide a reference for future improvement on the underwater laser sensing system and imaging system.

1.3 Research Objectives

The aim of this study is to investigate the influence factors to enhance the performance and quality of underwater single-pixel imaging. To achieve this, this study has been segregated into several research objectives, which is outlined below:

- 1) To investigate the medium effect on underwater light propagation. The medium effects including water turbulence, salinity concentration, and turbidity level.
- 2) To investigate the effect on image resolution, sampling ratio, water turbidity level, and laser wavelength on the performance of underwater single-pixel imaging.

1.4 Organization of Thesis

This thesis consists of a total of six chapters, including this chapter of introduction. The rest of the thesis is structured as below.

Chapter 2 provides a literature review for the research. It provides an overview and understanding of underwater imaging. This also includes the summary of findings of different underwater imaging techniques. This provides the basis of the study, investigation, and improvement work in the thesis.

Chapter 3 provides the theory, methodology, results, and discussion of the investigations in the medium effect of underwater light propagation. The analysis of each medium effect, including water turbulence, salinity, and turbidity, is provided in this chapter as well.

Chapter 4 provides the concept, methodology, results, and discussion of investigation in underwater single-pixel imaging quality. The study of the effect of image resolution, sampling measurements, and water turbidity, and laser source wavelength is summarized in this chapter.

Chapter 5 concludes the thesis with a summary of the research study and findings and recommendations on future work.

Chapter 6 provides the reference list used in this thesis.

2.1 Influence Factors and Considerations of Underwater Laser Sensing System

2.1.1 Laser Source and Profile

In a laser sensing system, the reflection intensity carries important information. Thus, it is important to have a complete and comprehensive understanding to improve system performance. Various researches have been done on the investigation of influence factors in the laser sensing system such as laser source [17], sensors in an underwater medium [18, 19], distance interference[20, 21], and scattering effect [22].

In 2016, Wang *et al.* studied the impact factor of the laser source profile on the underwater laser imaging system [17]. In the study, the triangular range-intensity profile spatial correlation method was proposed and utilized in underwater 3-D range-gated imaging. Underwater 3-D range-gated imaging has excellent potentials in long-distance, real-time, and high-resolution imaging compared to conventional 3-D laser scanning. Conventional underwater 3-D range-gated imaging operates by obtaining two gated images and reconstruct them based on the range-intensity correlation of the two overlapped gated images. In conventional 3-D range-gated imaging, the trapezoidal range-intensity profile is used by matching the temporal parameters. The trapezoidal range-intensity profile also using two times longer gate time comparing to laser pulse width. In the results shown by Wang *et al.*, the triangular range-intensity profile has a higher resolution than a conventional trapezoidal range-intensity profile and better real-time performance compared to the time-slicing method. Triangular range-intensity profile formed when gate time equals laser pulse width.

Bartolini et al. studied the use of amplitude-modulated laser radar at 405 nm wavelength in underwater 3-D imaging [23]. The proposed system consists of the micro scanning system and the diode laser source with a 405 nm wavelength. An amplitude-modulated laser source can reduce the backscattering effect of underwater light propagation. In the results shown, the system is well suited for underwater image reconstruction at clean or clear seawater due to the diode laser wavelength corresponding to the minimum absorption spectrum of pure water.

Recently, Kelly et al. studied the multiple wavelength laser beams propagating underwater medium [24]. The paper studied the performance of a red-green multiple wavelength beam and compared it with the performance of its component beams. The investigation has shown that the multiple wavelength laser beam will interact with variations in refractive index along with the beam propagation; this could ensure the receiver receives higher and more sustained saturation signals. The study also investigated the scenario with more kinetic turbulence. The reduction in intensity and amount of scintillation has increased with more kinetic turbulence, and the use of multiple wavelength laser beam has reduced the scintillation and ensure the higher intensity of light hitting the receiver.

2.1.2 Atmospheric Effects

Generally, the significant factors for signal reflectance reduction are the range and transmission medium. The reduction of signal reflectance is mainly due to the light scattering and absorption effect. Scattering and absorption of light are the fundamentals of inherent optical property (IOP), which is the property depending mainly on water and other dissolved substances or suspended particles in water. The relationship between absorption and scattering coefficients with water and substances in it can be described by the equations below[25]:

$$a(\lambda) = a_{dissolved} + a_{phy} + a_{CDOM} + a_{water} \quad (1)$$

$$b(\lambda) = b_{dissolved} + b_{phy} + b_{water} \quad (2)$$

The equations above describe the relationship of absorption ($a(\lambda)$) and scattering ($b(\lambda)$) coefficient in the water. Where the subscripts *dissolved*, *phy*, *CDOM*, and *water* are representing dissolved or suspended particles in water (biological and inorganic), phytoplankton (chlorophyll), colored dissolved organic matter, and water molecules. Based on the absorption coefficient of pure water data in [26], the absorption coefficient of pure water at a wavelength of 532nm is approximately 0.0447m^{-1} . Hou *et al.* stated the optimal transmission window of ocean water generally is around 550nm [27].

The total energy attenuation is based on the scattering and absorption in the water. The overall attenuation coefficient can be described as the equation below.

$$c(\lambda) = a(\lambda) + b(\lambda) \quad (3)$$

In 2016, Zheng et al. demonstrated an experimental setup for high speed and resolution objects imaging and detecting in the turbid underwater medium through logical stochastic resonance (LSR) [28]. LSR is the phenomenon of obtaining signals with noise and nonlinearity to increase the response accuracy. In underwater imaging, LSR can be utilized to extract detailed information from highly degraded and heavy noise images. Underwater images captured usually encounter heavy noise caused by suspended particles, especially in turbid underwater areas. In the study by Zheng et al., the LSR system takes an input signal of a normalized 1-D form of a highly degraded underwater image. Then, the object extracting from the background can be done by additional Gaussian noise.

Sluzek et al. proposed the application of adaptive fusion of gated imaging systems in highly scattering media such as turbid underwater areas [29]. Gated imaging systems can eliminate the noise caused by the backscattering signal by determining the timing of the target-reflected pulse. There are two signals obtained in the conventional imaging system: the backscattering signal and the target-reflected signal. Backscattering signal timing determination can be achieved with laser pulse information, while the distance between target and sensors determines the timing of the target-reflected signal. Then, gated imaging can eliminate backscattering signals with the information of the timing and only receive the desired signal, which is the target-reflected signal. In 2016, Lu et al. proposed an image restoration technique using spectral properties and light compensation in turbid areas [30]. The study introduced an underwater imaging post-processing technique, a fast-weighted guided normalized convolution domain filtering algorithm, which has the advantages of noise removal, and higher computation efficiency. The results show that the algorithm is suitable and effective in underwater imaging restoration without artificial light sources.

The theoretical study by Lu et al. provides an understanding of the behavior of partially coherent beams transmitting underwater medium with the effect of turbulence and salinity [31]. The study focused on the beam spreading on the propagation path. There are strong and weak turbulence areas in oceanic turbulence. The spreading of the coherent beam increases when propagating through a strong turbulence area and it is regardless of the strength of the beam. In comparison, the coherent beam with weaker coherence has even wider spreading and longer turbulence distance comparing to a stronger coherence beam in propagating through weak turbulence areas. The study also investigated the salinity concentration effect on beam spreading. The results have shown that the salinity fluctuation has a more significant contribution to beam spreading than temperature fluctuation.

Salinity concentration in seawater varies based on different depth levels and regions. Seawater optical properties are mainly based on the dissolved substances and constituents. The main dissolved substances in seawater are inorganic salts. In 2014, Zhao et al. published their experimental analysis on various chemical compositions in seawater to observe the refractive index change [32]. The experimental analysis involved the use of different wavelengths between 405nm to 633nm. From their experimental analysis, the refractive index decreases when the solution concentration and different with different chemical compositions. The relationship between solution concentration and the refractive index has been shown to be linear based on the experimental result. Different wavelengths of laser sources are used, and not many variations have been observed on the refractive index with different wavelengths (405nm to 633nm) used. In 2009, Zhang et al. proposed a theoretical model for estimating light scattering due to salinity concentration [33]. In the study, a theoretical model was proposed to relate the scattering strength at 90° with the salinity concentration fluctuation. Based on the result in the study, the simulation results match well with the experimental result with increasing light scattering at 90° at a higher salinity concentration level.

The study of influence factors of water turbulence is essential to ocean optic study as there is always turbulence occurring in the ocean. Thus, it is worthwhile to further investigate the effects of water turbulence as the result of the study could contribute to the improvement of the system performance. The turbulent impact caused by the refractive index variations leads to degradation of the beam quality and, therefore, the performance of the system. The modeling of a simple underwater imaging model relates to the combined impact of temperature and salinity microstructures. According to Hou et al., the strength of optical turbulence can be quantified based on the evidence of image degradation. By quantifying through optical conditions with absorption

and scattering and field turbulent conditions with turbulence kinetic energy dissipation rate (TKED) and temperature variance dissipation rate (TD), model closure can be achieved by partitioning image degradation based on particle and turbulence scattering. Results have shown that the degradation of image quality on a level just above thermocline by optical turbulence due to particle scattering [34].

Hanson and Lasher studied the impact on underwater laser transmission with the presence of turbulence [35]. In the study, collimated flat-top and Gaussian laser beams are transmitted in an underwater medium with turbulence generated by temperature fluctuations and flow from the circulating pump. They characterized the focused spots on the image. The results have shown that when the beam radius with approximate transverse coherence length, the lesser degrading effect of turbulence due to high coupling efficiency. The experimental analysis is consistent with a theoretical study based on the Kolmogorov spectrum of refractive index fluctuations.

According to Mahdiah *et al.*, changes or variations on the propagated beam quality will occur when a laser beam is transmitted through turbulence [36]. The research expressed the beam quality or beam propagation factor, M^2 . The propagation will cause distortion on the beam phase front and eventually leads to variations in beam propagation direction and intensity fluctuations (Scintillation index). The scintillation index is an essential understanding for many applications as it allows the categorization of the turbulence strength [37]. The study shows the beam quality (higher M^2 factor) has decreased with increasing turbulence strength at different distances.

The thermal blooming effect is when a fraction of beam energy is absorbed after propagated through a medium and causes alteration of the refraction index of the path. This distorts the beam and eventually affecting the laser reflections. Zhang et al. studied the thermal blooming effect of underwater laser transmission by utilizing a numerical simulation method [38]. The study has

shown that the thermal blooming effect becomes worse and more obvious as salinity concentration increases. Furthermore, the study investigated the thermal blooming effect corresponding to the wavelength used. The results have shown that the wavelength with a higher absorption coefficient has a more significant thermal blooming effect.

The choice of laser to be utilized in the underwater medium is much dependent on the water absorption as the attenuation effect is the main issue of underwater imaging. The attenuation effect consists of absorption and scattering, and the wavelength of the blue-green laser is shown to be the transmission window in seawater with a minimum attenuation effect [39]. However, there is strong investigation evidence that shows no more than 10% variations between the absorption coefficient for both fresh and seawater for wavelengths longer than 375nm [40, 41]. According to Wang et al. [42], the absorption coefficient and travel distance of red light (between 600nm and 700nm) are higher compared to green and blue light with a shorter wavelength, and this agrees well with the previous study. The study by Wang et al. has shown that the blue and green light with shorter wavelengths will have more scattering than the red light, which is a longer wavelength based on Rayleigh scattering theory.

2.2 Underwater Imaging

2.2.1 Overview of Imaging System

The imaging system can be categorized into two categories: active and passive imaging. Active imaging utilizes a system-generated light source, while passive imaging uses external system-generated or natural light sources such as sunlight. Active imaging is compelling and exciting among researchers in underwater imaging due to insufficient light in the deep-sea region. There

are various techniques and technologies applied in underwater imaging in the past few years. The range-gated method is a cost-effective and affordable technique due to the increasing usage of laser, sensors, and computing systems. Green pulsed laser source with a low repetition rate has been continually utilized to improve image contrast by reducing the backscattering of light propagation [43].

The range-gated imaging system mainly consists of a pulsed laser as the source to the target and a gated camera as the sensor in the system. Range gated imaging operates based on the time of flight (TOF) principle. TOF principle is used by measuring the round trip time of the transmission between the source and target. The range-gated method also provides a high sampling rate for reconstructing 3-Dimensional (3-D) imaging from numerous short time slices [44]. Generally, the range-gated method is suitable for fast scanning and long-distance applications because of its high speed of light [45]. This technique allows optically suppressing background noise by controlling active light source illumination and gate exposure time. The suppression of the backscattering light from the atmospheric effect such as fog and smokes etc., allows penetration through obscurants. However, power efficiency, low resolution, and accuracy are the significant drawbacks of the range-gated method. The range-gated method requires an entire scene of light source illumination for every time slice [46]. Moreover, the range-gated method has the limitations of low resolution and accuracy due to the target reflectivity and illumination effect [47], sensor effect [19], and image quality due to target speckle [48].

The laser line scan method (LLS) scans the narrow field of view linearly with the receiver synchronously. LLS method allows for reducing scattered light spatially to improve imaging quality [43]. However, the LLS method is limited by receiver noise caused by temporal overlap between the reflected and illuminated light, including solar and laser sources. LLS method with

continuous-wave and increased separation of source and receiver have been utilized to maximize the operational range by reducing the detrimental multiple scattered light effects [49, 50]. The pulsed laser line scan method (PLLS method) is an LLS method with a high repetition rate pulsed lasers and gating sensor. This method reduces the light beam overlap effects, improves the image contrast and system operational range by temporal separation of the target signals and scattered light [51]. The other limitation of the LLS method is the low efficiency of the system. The line-by-line scanning of the LLS method causes a slow sampling rate of the system.

Structured light imaging illuminates a known light pattern onto the target, and the target distorts the light pattern. The light pattern distortion carries info for reconstruction for 2-D and 3-D surface topography. The distance-compensated technique is known to be applied in structured light imaging to improve the contrast over wide-field illumination [52]. Moreover, synthetic aperture illumination is also known for commonly utilized with structured light imaging. Synthetic aperture illumination uses multiple illumination sources from various positions and directions [53]. Thus, this creates multiple frames, and different sets of illumination patterns are created. However, the multiple illumination sources cause backscattered light similar to wide-field illumination. Thus, the backscattering effect is required to be compensated by post-processing to improve image quality. The structured light imaging system has better measurement coverage when the distance is fixed but with drawbacks such as limitation of the field of view and obtaining pixel-level resolutions [54].

Single-pixel imaging acquires images by sampling scenes with spatially resolved patterns and measuring the corresponding intensity from the detector without spatial resolution. Thus, single-pixel imaging reconstructs the entire image by scanning a single-pixel to detect intensity information from a scene [55]. This reduces the waste of data storage and the time of sampling

compared to conventional applications [56, 57]. Single-pixel imaging is also a cost-effective and affordable method due to increasing development in sensors and quantization electronics. However, Duarte et al. showed that there is a trade-off of significant mean square error from the advantages and the dynamic range of the detectors [57]. Moreover, instead of one-shot reconstruction using a detector array in the conventional imaging system, single-pixel imaging reconstructs an image with only one detection element, and the reconstruction to be performed sequentially for some time. Thus, high-speed electronics, high computational power, and fast modulating spatial light modulator (SLM) are required to compensate for the long computing process of a single-pixel imaging system [58].

Table 1 Summary of advantages and drawbacks for the conventional imaging system.

Methods	Advantages	Drawbacks
Range-gated Method	<ul style="list-style-type: none"> ➤ Fast speed or high sampling rate ➤ Cost-effective ➤ Able to operate over a long distance 	<ul style="list-style-type: none"> ➤ Power inefficiency ➤ Sensor effect ➤ Target and illumination effect
Laser Line Scanning Method	<ul style="list-style-type: none"> ➤ Able to reduce the scattered light effect ➤ System operational range 	<ul style="list-style-type: none"> ➤ Slow sampling rate
Structured Light Imaging	<ul style="list-style-type: none"> ➤ Fast speed or high sampling rate ➤ Cost-effective 	<ul style="list-style-type: none"> ➤ Limited field of view ➤ Low resolution ➤ Complex in computation
Single-pixel Imaging	<ul style="list-style-type: none"> ➤ Cost-effective ➤ Low data storage requirement ➤ Fast sampling rate 	<ul style="list-style-type: none"> ➤ Low resolution ➤ Low accuracy

2.2.2 Underwater Imaging System

Cai et al. studied the application of compressive sensing in underwater sonar image processing [59]. In the study, the Bandelets transform and Gaussian random matrix are used as sparse image representation and observation matrix, respectively, then image reconstruction using the Orthogonal Matching Pursuit algorithm. Bandelets transform is effectively in edge and contours preserving compared to wavelet basis with the same sampling rate. The results have shown that the proposed method improves data acquisition efficiency, transmission efficiency, and image reconstruction accuracy.

The study by Ouyang et al. proposed a compressive sensing-based underwater laser serial imaging system with the potentials of lesser system cost, compactness, and better system reliability and flexibility [14, 60, 61]. The proposed technique is compared with the structured illumination and laser line scan (LLS) system in the study. The results have shown that the compressive sensing technique has better photon efficiency than structural illumination due to compressive sensing utilizes a Photomultiplier tube (PMT) to detect photons reflection generated by DMD. Although the compressive sensing technique requires computation-intensive optimization, compressive sensing has a faster imaging speed than structural illumination and LLS.

In 2019, Chen et al. proposed the application of single-pixel imaging with compressive sensing in an underwater medium to overcome the drawbacks of conventional single-pixel imaging, including low reconstruction quality, efficiency, and long data-acquisition time [62, 63]. In the study, a compressive sensing-based single-pixel imaging system is utilized to reconstruct a 2-D transparent object. In the results shown, the compressive sensing-based reconstruction technique reduces up to 70% data acquisition time compared to conventional single-pixel imaging algorithm.

Moreover, the compressive sensing-based reconstruction method shows reconstruction capability even at a turbidity level of 80 Nephelometric Turbidity Unit (NTU).

2.3 Single-pixel Imaging

2.3.1 Overview of Single-pixel Imaging

Single-pixel imaging systems mainly contain two parts: acquisition (the process of performing measurement or data obtaining) and reconstruction (computing process to rebuild or restore the image). A greyscale image is a 2-D array mathematically, and the value of each array element representing the reflectivity measured from the target at the corresponding array spatial location. The 2-D array image can be converted into a 1-D array, or image, $I = [i_1, i_2, i_3, \dots, i_N]^T$. In this study, the conversion of the 2-D array to the 1-D array used is the row-major ordering, as shown below in Figure 1.

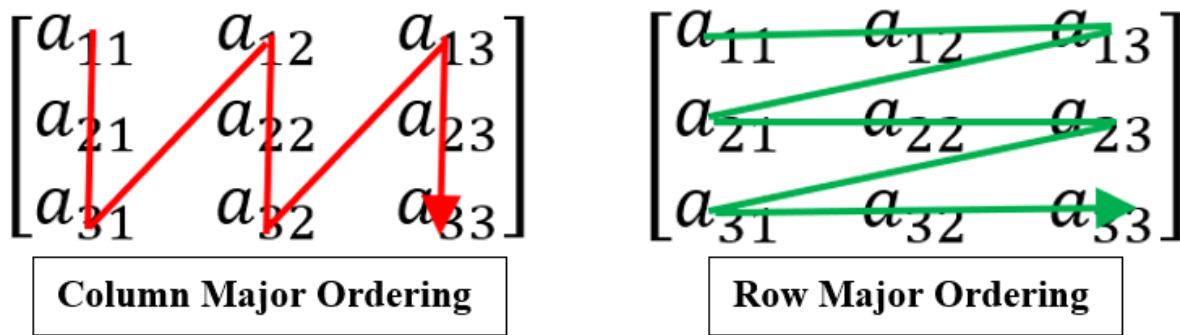


Figure 1 Column and row-major ordering

In old times, raster scan imaging was the most straightforward method by measuring the reflectivity value of array element once at a time, and the single-point scanning method is time-consuming due to image formation time proportional to the number of image pixels, N . Thus, modern digital cameras measure N elements simultaneously with detector array with N elements. However, detector arrays for unconventional spectrums and applications are costly or unavailable such as ultraviolet and time-correlated single-photon counting [58]. In single-pixel imaging, the SLM modulates the image array, I with an illumination pattern P_i , and the total reflected or transmitted light intensity are detected and measured by the single-pixel detector,

$$S_i = P_i * I \tag{4}$$

Similarly to image I , where $P_i = [P_{i1}, P_{i2}, P_{i3}, \dots, P_{iN}]$ is a 1-D array converted from the 2-D array. The linear equation below can be obtained after the single-pixel imaging system obtains M measurements

$$S = P * I \tag{5}$$

where $S = [S_1, S_2, S_3, \dots, S_M]^T$ is a 1-D array obtained from M measurements, and P is a 2-D measuring matrix of $M * N$ array. Mathematically, to solve N independent unknowns and reconstruct image I , there two requirements to meet, (i) $M = N$ and (ii) P is orthogonal,

$$I = P^{-1} * S \tag{6}$$

Due to major natural scenes are sparse or compressible with wavelet transform (WT), P can be represented by the sparse matrix. Moreover, many sparse-based measuring matrices created are orthogonal as well, including wavelet pattern [64, 65], Hadamard pattern [66, 67], and Fourier pattern [68, 69].

The single-pixel imaging system's performance depends on the performance of the single-pixel detectors and SLM in combination. There are various SLM technologies used in single-pixel imaging system including rotating ground glass [70, 71], customized diffuser [72, 73], liquid-crystal device (LCD) [56, 74], light-emitting diode (LED) array [75, 76], digital micromirror device (DMD) [77, 78] and optical phased array (OPA) [79, 80]. The spatial resolution of the pattern is important in the single-pixel imaging system. Every SLM device has its limitations on spatial resolution, such as 1074×768 for DMD. The programmability of the illumination pattern of the SLM device offers flexibility in sampling, such as LCD, LED array, and DMD. This could improve the overall system performance in regional resolution [81] and SNR [66].

Rotating ground glass and customized diffusers operate in a spectrum based on the lens material used. In contrast, LCD and DMD operate in the bandwidth of wavelength depending on their properties of transmissive and reflectivity. Moreover, LED array and OPA are usually working in narrow-band wavelengths, and the operating spectrum is based on the light-emitting component [58].

Data acquisition time is a significant factor in selecting the SLM device as well due to acquisition time is the product of the patterns switch time and measurements M required. DMD has been known for being commonly used as an SLM device in single-pixel imaging, which has a typical modulation rate of $22kHz$. It requires a data acquisition time of $46.5 ms$ for a 32×32 pixel resolution, giving a frame rate of $21 fps$ (frame-per-second). The application requires a

faster modulation rate, the LED array, and OPA with a fast-switching photonics module that can reach over one *MHz* [76, 79].

Table 2 Summary of advantages and drawbacks of the modulation method of single-pixel imaging.

Modulation Method	Advantages	Drawbacks
Rotating Ground Glass	<ul style="list-style-type: none"> ➤ Low in cost ➤ High power endurance 	<ul style="list-style-type: none"> ➤ Non-programmable ➤ Random modulation pattern only
Customized Diffuser	<ul style="list-style-type: none"> ➤ Customizable ➤ High power endurance 	<ul style="list-style-type: none"> ➤ Non-programmable ➤ Complex in manufacturing
LCD	<ul style="list-style-type: none"> ➤ Programmable ➤ Greyscale modulation available 	<ul style="list-style-type: none"> ➤ Low power endurance ➤ Slow modulation rate
LED	<ul style="list-style-type: none"> ➤ Programmable ➤ Very high modulation rate 	<ul style="list-style-type: none"> ➤ Binary modulation ➤ Structured light illumination only
DMD	<ul style="list-style-type: none"> ➤ Programmable ➤ High modulation rate 	<ul style="list-style-type: none"> ➤ Binary modulation
OPA	<ul style="list-style-type: none"> ➤ Controllable ➤ Very high modulation rate 	<ul style="list-style-type: none"> ➤ Binary modulation ➤ Complex in manufacturing

2.3.2 Applications

Underwater Imaging

The active imaging system is one solution for darkness or low light region such as underwater mediums. Underwater imaging with single-pixel imaging has been researched widely throughout the years due to the advantages of disturbance-free and the ability to capture an image in poor conditions, including low light, high absorption, and backscattering conditions [62, 63, 82, 83]. Chen et al. have presented underwater single-pixel imaging with compressive sensing with more elevated reliability in hidden objects imaging than conventional imaging approach [82]. The application of compressive sensing has reduced the data acquisition time and measurement for the same resolution level achieved by conventional single-pixel imaging algorithm. In the study [63], a single-pixel imaging system has shown better results with lesser influence by underwater turbidity effect than the gated conventional imaging system. Wu et al. proposed a polarization-based single-pixel imaging system to reduce the backscattering effect in an underwater region [83]. The proposed technique was inspired by the polarization-based de-scattering technique to eliminate the backscattering effect by applying two cross-polarization single-pixel imaging detection schemes.

3-D Imaging

3-D imaging has been an exciting topic among researchers, with applications in security, robotics, and medical science [54, 84, 85]. There are various approaches in 3-D single-pixel imaging, including the time-of-flight (TOF) and stereo vision approach [58, 86, 87]. In 3D single-pixel imaging with a stereo vision approach, two or more images are recorded simultaneously from different angles and perspectives of the scene for 3-D image reconstruction. 3-D image reconstruction is done by associating the measured light intensity and the geometry information from different views. However, the reconstruction with geometry registration between images from different viewpoints can be complicated.

One illumination pattern corresponds to one measured light intensity only in a 2-D single-pixel imaging. However, in 3-D single-pixel imaging with TOF, one illumination pattern corresponding to several series of measured light intensity at different depths can be achieved with a pulsed light laser source and a time-resolving detector. A series of images can then be reconstructed with the illumination patterns and the measured light intensity at different depths. Finally, the 3-D image can be reconstructed by extracting the depth and reflectivity information of the scene from the data in the image. Compared to a stereo vision approach, 3-D single-pixel imaging with the TOF approach has the advantage of absolute distance measurement, indicating depth resolution is unaffected by increasing distance. Thus, 3-D single-pixel imaging with the TOF approach is suitable for long-distance 3-D measurement applications.

Surface Inspection

Surface inspection is an important industry application to inspect the surface defect and morphology. First, the time-stretch-based single-pixel imaging (TSSPI) system can detect surface defects in micrometer-sized with high-speed scanning and inspection [88, 89]. TSSPI uses infrared wavelength and can generate illumination patterns at high speed. This is done first by breaking up the broadband optical pulse and then shaping the stretched optical pulse spectrally with time-encoding. The illumination patterns can be formed by wavelength-to-space mapping in a spatially dispersive medium. Thus, the pattern generation rate can reach beyond ten *MHz*. The study also shows the decrease trend of peak signal-to-noise ratio (PSNR) with a lower compression ratio, indicating a better reconstruction result requires a higher number of measurement data [90]. The high-speed surface inspector can be applied in an organic light-emitting diode (OLED) display manufacturing industry to improve the cost-effectiveness and performance of the manufacturing process.

Chapter 3 Medium Effect on Underwater Light Propagation

This chapter presents the experimental investigation of effects of various factors, including water turbulence, salinity, and turbidity. The experimental setup and procedure of the investigation of the medium effect on underwater light propagation are described in Section 3.1 and Section 3.2. A detailed experimental results and discussion are presented in Section 3.3.

3.1 Experimental Setup

Experimental setup, as shown in Figure 2, is used for the investigation of various influence factors in the underwater imaging system. Theoretically, each pixel exhibits the same characteristics as the reflected laser pulse, where the LADAR principles apply. Therefore, this study uses the photodetector for reflected laser investigation where some effects are excluded, for instance, the DMD efficiency and noises.

This setup uses a pulsed laser source to emit laser to hit the target through the beam splitter. A beam splitter is used to split the incident laser beam onto photodetectors and targets. The target is placed in a water tank, and the variations of turbulence strength can be achieved by controlling the water outflow rate in front of the target. Moreover, the salinity concentration and turbidity level can be achieved by controlling the concentration of fine salts and cement added into the water tank, respectively. The photodetectors detect reflected laser signals and are connected to an oscilloscope to obtain the peak data during the experiment. A mirror is used as the target, and the distance between the target and laser source is fixed at a distance of 1 meter in this study. The experimental data are used for range accuracy evaluation to determine system performance. Figure 3 shows the experimental setup of the underwater ranging system. The system consists of a 532nm pulsed laser

emitter, 1 inch 50/50 beam splitter, mirror, model 818-BB-21 high-speed photodetectors, and Rigol DS6104 digital oscilloscope.

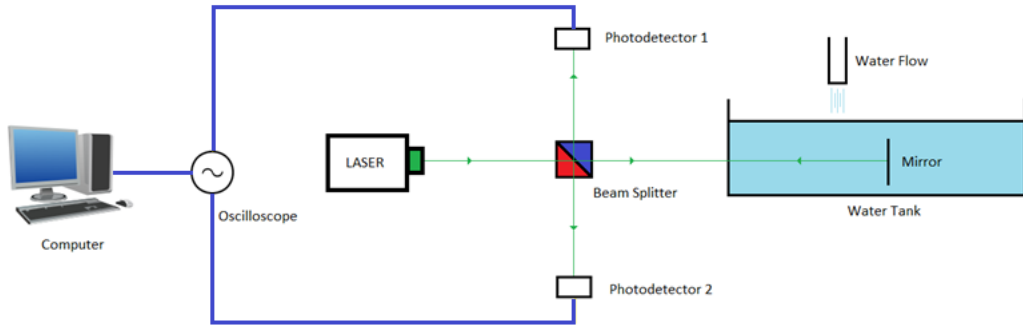


Figure 2 Schematic diagram of underwater laser ranging system experimental setup.

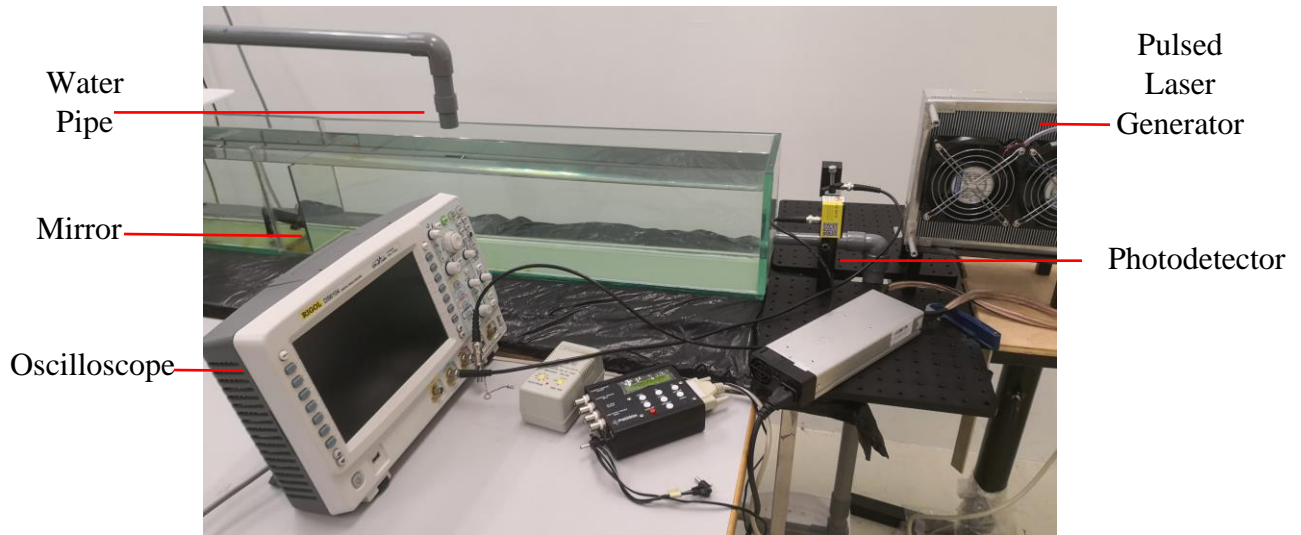


Figure 3 Experimental setup of underwater pulse ranging system

3.2 Experimental Procedures

3.2.1 Data Collection

The electrical signals data of illumination and reflection, as shown in Figure 4, is collected for evaluating reflection ratio (in/out) and range error. The electrical signal detected and shown in purple color represents the signal detected from the laser source. Thus, the amplitude is higher than the reflections signal detected due to losses. The electrical signal in blue color represents the signal detected from reflections after hitting the target. Based on Figure 4, the first amplitude is higher than the second amplitude detected. The first amplitude is due to the reflections on the tank. The second amplitude is due to the reflections on the target. The lower amplitude mainly due to the underwater water turbulence, salinity concentration, and water turbidity effect. To further understand the impact of water turbulence on underwater light propagation, the reflection ratio, which is the ratio of the amplitude of reflections to the amplitude of the source, is obtained and analyzed.

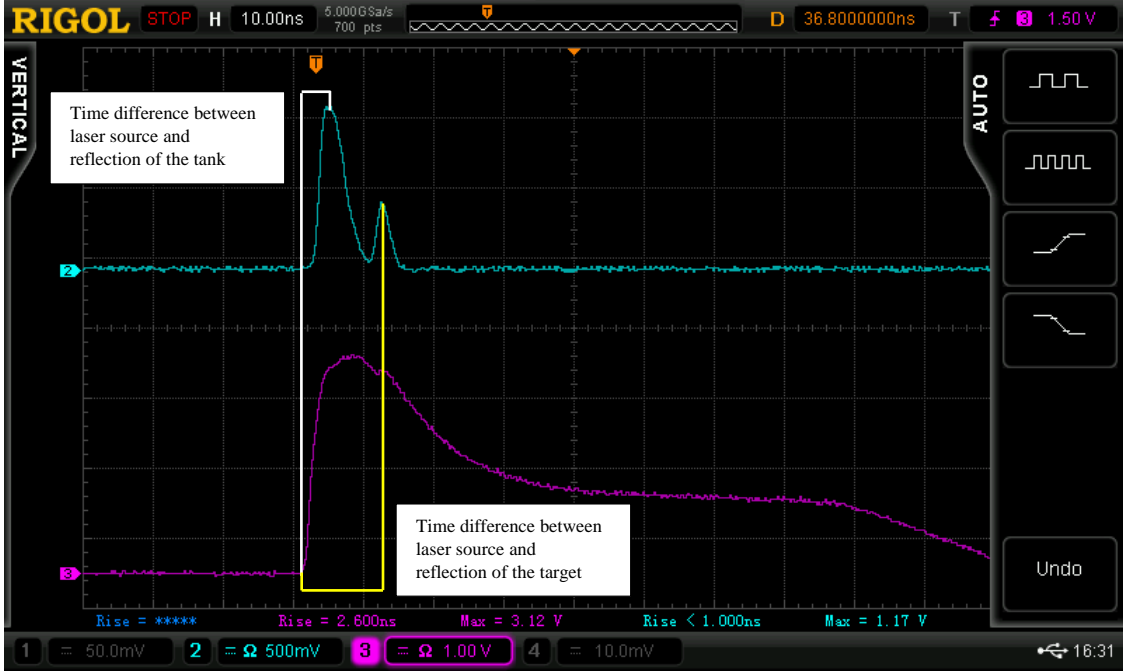


Figure 4 The electrical signals detected from the oscilloscope. The electrical signal is shown in purple color representing the laser source signal, while the electrical signal in blue color representing the reflection detected after hitting the target.

3.2.2 Reflection ratio

LADAR range equation has described the relationship between emitted and returned laser energy [91]. There are various influence factors on the returned laser energy in a ranging laser system; the total returned optical power equation is given by:

$$P_r = \frac{\eta_{sys} \eta_{atm} D^2 \rho A P_s}{r^2 \theta_R (\theta_t r)^2} \quad (7)$$

where P_r and P_s are the received and transmitted power from the target across the range, r . D , ρ , and A representing the sensor aperture area, reflectivity of target and target area, respectively. η_{sys} is the loss factor due to receiver optics transmission, while η_{atm} is the atmospheric loss factor due

to absorption and scattering. θ_R and θ_t are the laser beam diameter and the viewpoint of the receiver, respectively.

In the assumption of using a well-resolved target, the target object size is the same as the laser beam projected area:

$$A = \frac{\pi\theta_t^2 r^2}{4} \quad (8)$$

With the assumption, the reflection ratio can be simplified and expressed as below:

$$\frac{P_r}{P_s} = \frac{\pi\eta_{sys}\eta_{atm}D^2}{4r^2} * \frac{\rho}{\theta_R} \quad (9)$$

$$\frac{P_r}{P_s} = \text{Reflection Ratio} \quad (10)$$

$\frac{\pi\eta_{sys}\eta_{atm}D^2}{4r^2}$ corresponding to overall factors contributing to energy loss, and $\frac{\rho}{\theta_R}$ corresponding to target reflection characteristics.

3.2.3 Range Determination

The critical application of the LADAR system is the measurement of the range between target and source. The performance of the LADAR system can be determined by evaluating the range accuracy. The range, r is resolved by applying the time-of-flight (TOF) principle, as shown below:

$$r = \frac{ct}{2} \quad (11)$$

Where c and t are the speed of light in vacuum and time, respectively. In a LADAR system, the range, r is expressed as a two-way range as the time is recorded between the detection of emitted

and reflected laser pulse signal by a sensor. Moreover, the speed of light in the water medium is used in the equation instead of the speed of light in a vacuum in an underwater LADAR system. Thus, the range evaluation equation for an underwater LADAR system can be expressed as below

$$r = \frac{c_w \Delta t}{2} = \frac{c \Delta t}{2n_w} \quad (12)$$

where the n_w is the refractive index of water.

3.3 Results and Discussion

3.3.1 Water Turbulence Effect

The range error against turbulence strength is shown in Figure 5. The range error is the difference between the actual range and calculated based on the TOF principle. Figure 5 shows that the range error does not vary with the water turbulence strength as no trend can be observed. The range error evaluated shows consistently between 12% to 15% with different turbulence strengths in the water. This is due to the laser carries intense propagation energy to reach the target and detectors. Thus, it shows that range error does not correlate with turbulence strength as range error shows no significant changes with variation of turbulence strength due to range error would not be affected significantly by reflected intensity.

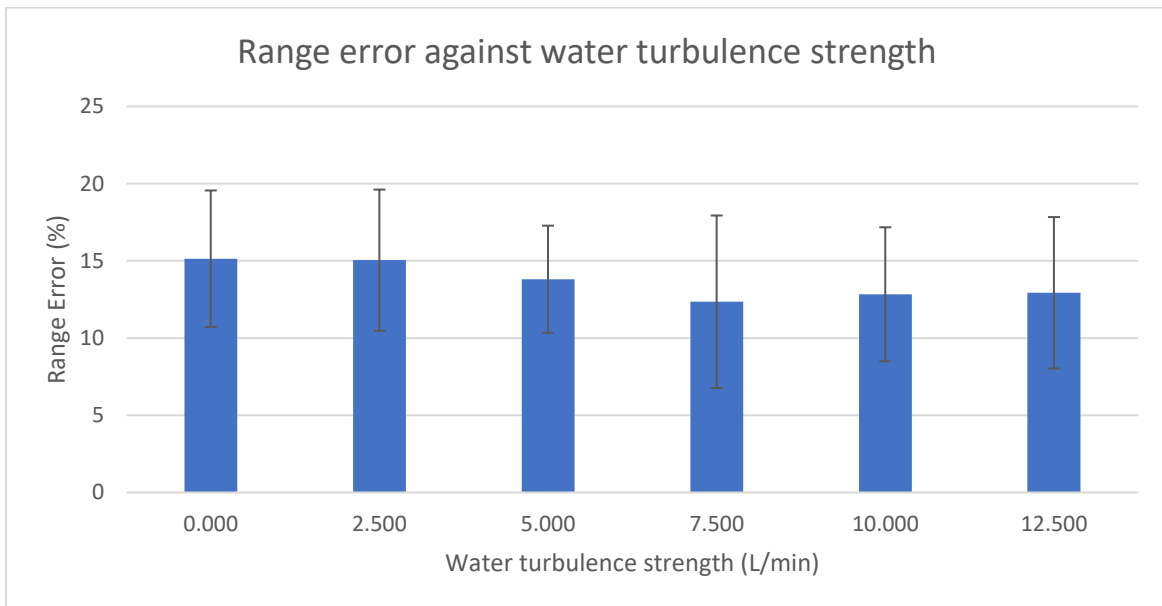


Figure 5 The range error obtained experimentally against different water turbulence strength (L/min)

According to Mahdiah et al., changes or variations on the propagated beam quality will occur when a laser beam propagates through turbulence [36]. The beam quality of beam propagation factor, M^2 is described using the following equation:

$$M^2 = \frac{\pi}{\lambda} w(x) \sqrt{\theta^2(F) - \frac{w^2(x)}{r^w(x)}} \quad (13)$$

Where λ is the wavelength. W and r are the beam width and radius, respectively. The report has also expressed turbulence strength as C_n , and the beam quality can be evaluated by the relation stated above. Finally, the turbulence strength, C_n can be estimated as well by relating M^2 factor. The propagation will cause distortion on the beam phase front and eventually leads to variations in beam propagation direction and intensity fluctuations (Scintillation index). The scintillation index is an essential understanding for many applications as it allows the categorization of the turbulence strength [92]. Thus, Mahdiah et al. show the beam quality (higher M^2 value) will decrease, and light propagation is weaker with stronger turbulence strength as the turbulence has caused distortion on the light beam propagation and leads to losses in reflectance.

The reflection ratio against turbulence strength is shown in Figure 6. Figure 6 shows that the reflection ratio decreases with higher water turbulence strength. Comparing the results in Figure 6 with the theoretical study by Mahdiah et al., it can be seen that the experimental results obtained match well with the theoretical work. This could be explained by the turbulence in the water to increase the refractive index and cause the weakening of the light intensity passing through.

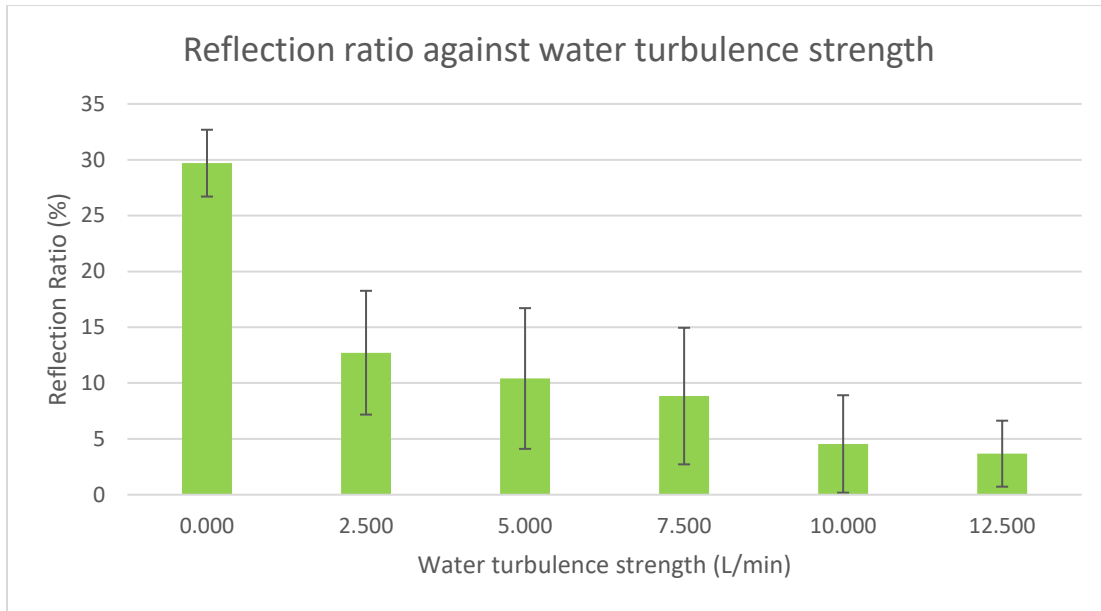


Figure 6 The reflection ratio obtained experimentally against different water turbulence strength

LADAR model shows the change in reflection intensity of light is contributed by various factors, including sensor, object target, source, and medium parameters. Theoretical studies of the water turbulence effect have shown that the beam quality decreases with stronger turbulence strength. The turbulence in water has caused distortion and variation on light beam propagation and eventually leads to reflectance losses. Our experimental results show a similar trend with the theoretical findings.

3.3.2 Water Salinity Effect

Figure 7 shows the range error against salinity concentration. It can be seen that the range error does not vary much with the water salinity concentration. The range error shows slightly up and down and unpredictable as the salinity concentration increases. The range error evaluated shows no noticeable trend as the range error remains 10% to 11% with different salinity levels in the water. This shows the range accuracy does not correlate with salinity concentration because the reflected intensity is insignificant in ranging performance. This is because the laser possesses enough energy to reach the detectors even with more particulates in the water.

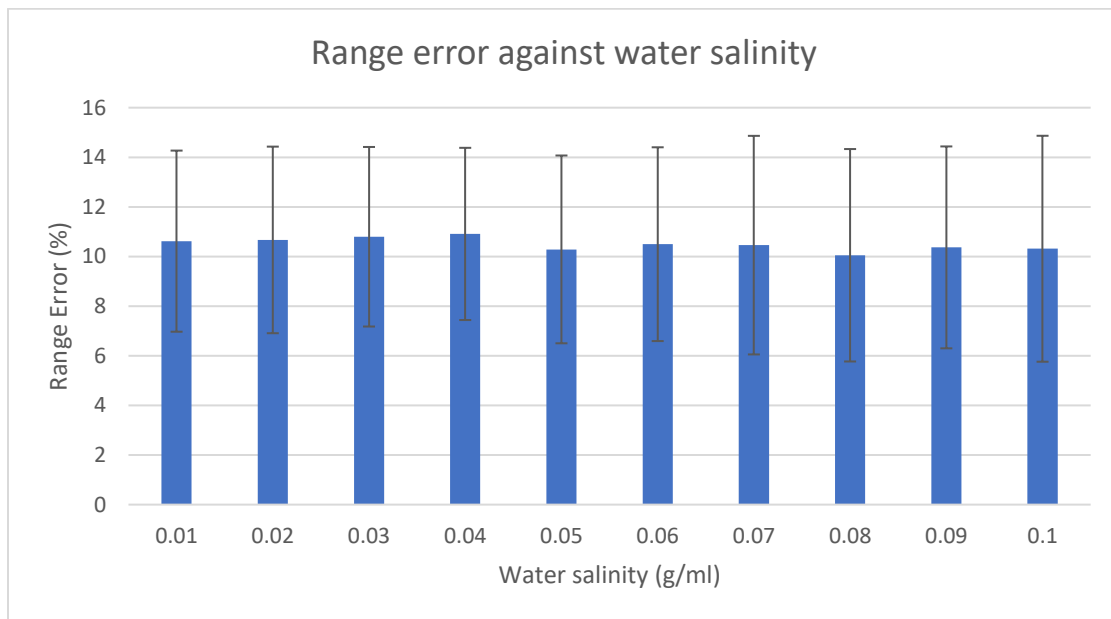


Figure 7 The range error obtained experimentally against different water salinity concentration(g/ml)

Figure 8 shows the reflection ratio against salinity concentration. The reflection ratio decreases with higher water salinity concentration, which representing lesser light intensity detected.

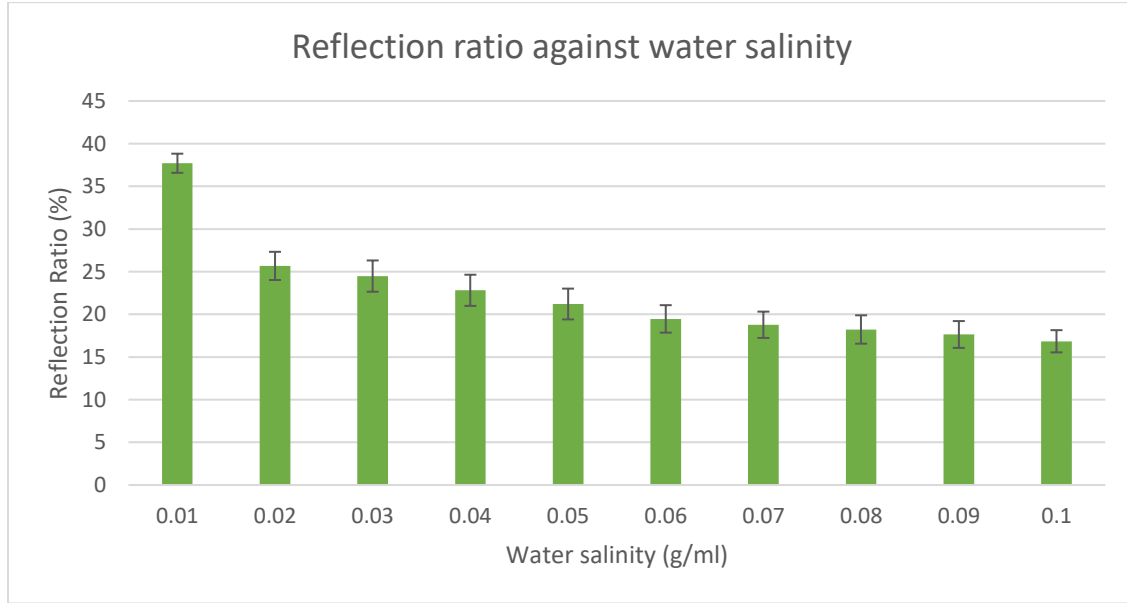


Figure 8 The reflection ratio obtained experimentally against different water salinity concentration (g/ml)

In 2009, Zhang et al. proposed a theoretical model for estimating light scattering due to salinity concentration [93]. The theoretical model shown below relates the scattering strength at 90° and the salinity concentration fluctuation:

$$\beta_c(90) = \frac{\pi^2}{2\lambda^4 N_A} \left(\frac{\partial n^2}{\partial c} \right)^2 \frac{c \bar{V}_o}{\partial \ln a_o} f(\delta) \quad (14)$$

Where $\beta_c(90)$ representing the scattering (at 90°) due to salinity concentration and N_A representing Avogadro number. n and c corresponding to refractive index and salinity concentration fluctuation. a_o and \bar{V}_o are the activity and molar volume of the solvent where the solvent is salt in this study.

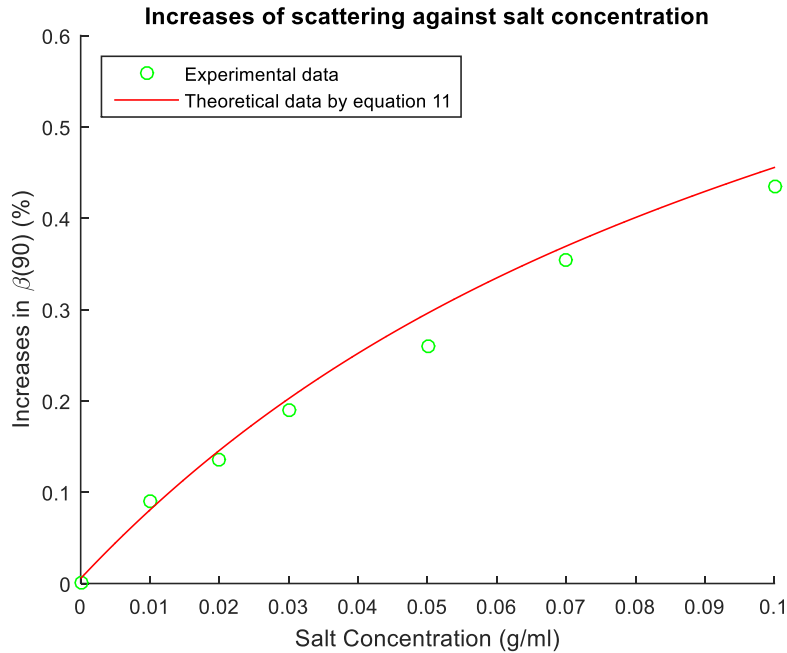


Figure 9 Zhang et al. has compared the experimental result with the proposed theoretical model (equation 14) [93]

In Figure 9, it shows the increasing trend of scattering effect when salt concentration increases based on the experimental result by Zhang et al. The research also shows the theoretical model proposed (equation 14) agrees well with the experimental study by Zhang et al.. Thus, the theoretical and experimental study by Zhang et al. shows the increases of scattering (90°) with increasing salt solution concentration in the water.

By relating the theoretical studies above and data obtained in Figure 8, it shows that the experimental results match with the theoretical result. This is mainly due to the scattering effect caused by the salt particulates in the water. As the salinity concentration increases, more particulates are in the water and causing more scattering effects occurring in the water. This is eventually causing higher variations and losses along with the laser beam propagation.

Theoretical studies of salinity concentration effect on underwater light beam propagation have shown a scattering of light in water increases with higher salinity concentration. The higher salinity concentration leads to a higher scattering effect due to more minor particulates in the water. Thus, it shows that our experimental results have shown a similar trend with the theoretical findings.

3.3.3 Water Turbidity Effect

Figure 10 shows the range error against the water turbidity level. The range error is growing exponentially with high turbidity levels in the water. This is mainly due to the high scattering and absorption effect in a high turbidity level medium. As the laser propagates through the medium, the laser power has been dissipated by light scattering and absorption effect and causing the delay of the reflecting signal.

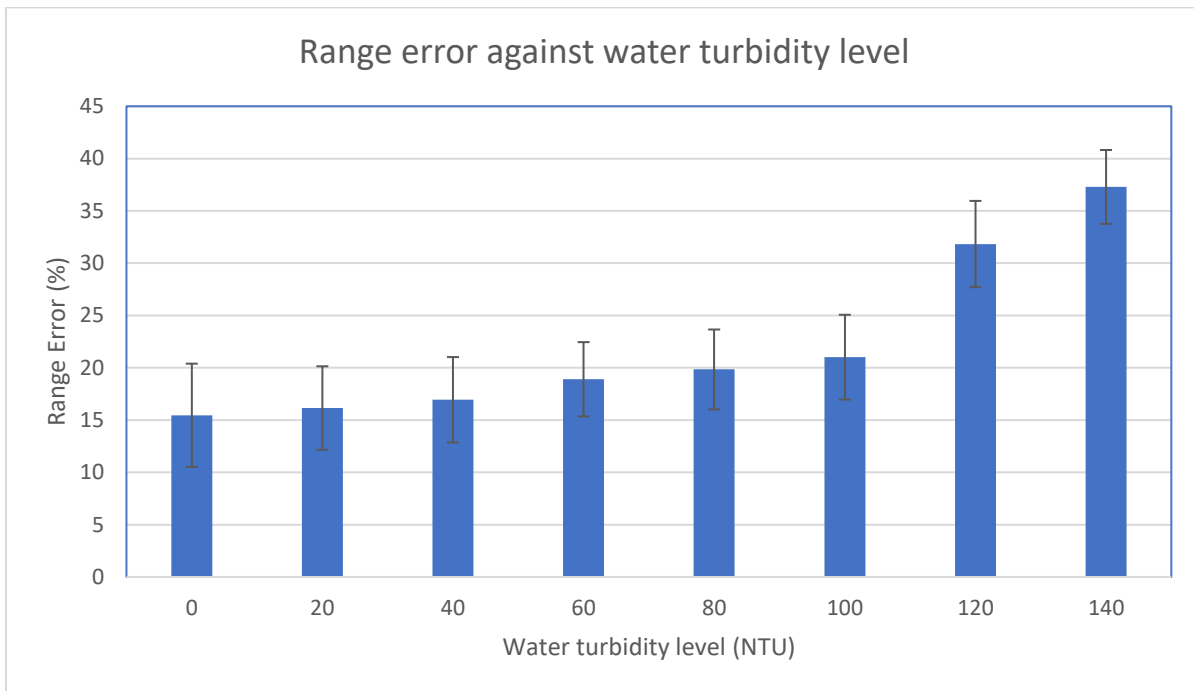


Figure 10 The range error obtained experimentally against different water turbidity level (NTU)

Figure 11 shows the reflection ratio against the water turbidity level. The reflection ratio decreases with higher water turbidity level, which representing lesser light intensity detected.

Based on the study by Chen et al. [62], the relationship between system accuracy with medium attenuation coefficient and target distance in a pulse ranging system can be shown with:

$$\eta_a = T(R) = e^{-cR} \quad (15)$$

Where η_a is the atmospheric loss factor, c is the attenuation coefficient in the medium, and R is the target distance. By relating the LADAR model and BRDF theory, A is defined as the impact factor of intensity error, which relates the parameters c and R . A can be written as:

$$A = \frac{\eta_a^2}{R^2} = \frac{(e^{-cR})^2}{R^2} \quad (16)$$

It shows that the impact factor decreases with a higher attenuation coefficient and target distance. In other words, the higher the attenuation coefficient, the lesser the returned laser power. Thus, in a medium with a higher turbidity level, the higher the medium attenuation coefficient and cause lesser the reflected laser power in the medium.

Comparing the theoretical study above and experimental results obtained in Figure 11 shows that the experimental results have a similar trend with the theoretical work. This is mainly due to the higher scattering and absorption effect in a higher turbidity level medium. As the water turbidity level increases, more particulates are in the water and cause more light scattering and absorption effects occurring in the water. This eventually causes higher variations and losses along with the laser beam propagation.

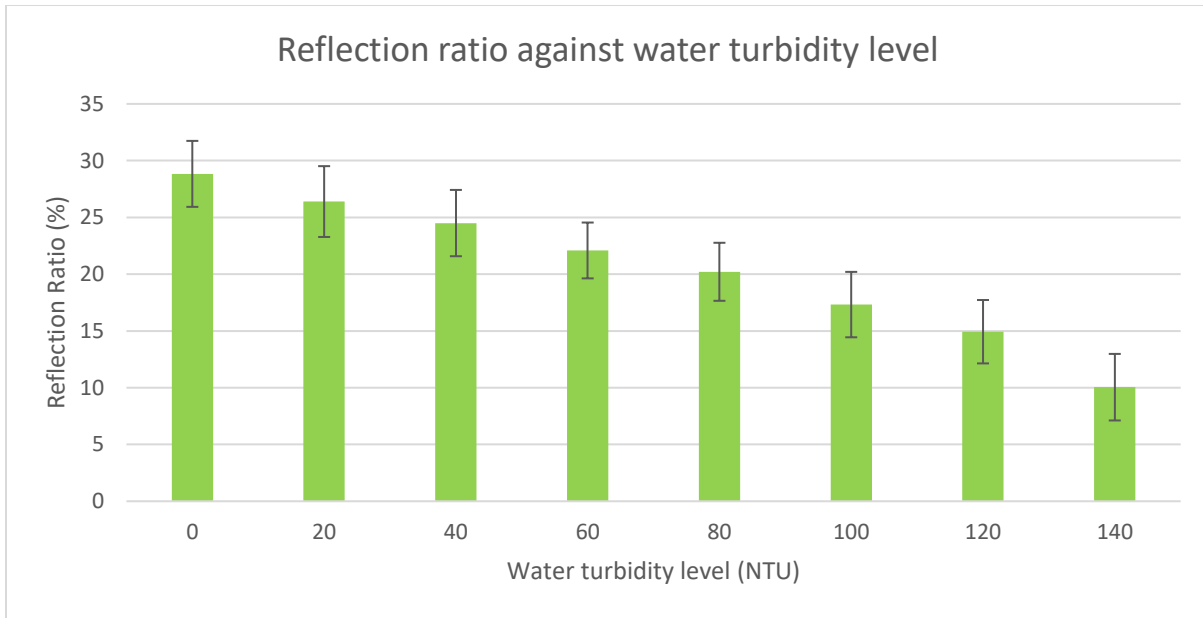


Figure 11 The reflection ratio obtained experimentally against different water turbidity level (NTU)

Theoretical studies of medium attenuation coefficient effect on underwater light beam propagation have been shown to affect the reflected signal's intensity and power. The higher water turbidity concentration leads to higher scattering and light absorption with more minor particulates in the water. Thus, it shows the experimental results have a similar trend with the theoretical findings.

3.3.4 Summary

The effects of water turbulence, salinity, and turbidity on underwater light propagation are investigated. The reflection ratio and range error accuracy were analysed. The reflection ratio shows an inversely proportional trend with water turbulence, salinity, and turbidity effects. The reflection ratio of reflected intensity shows the most considerable reduction in the water turbidity effect. The range error shows consistent and no significant variations with the increase of water turbulence and salinity. However, the range error shows an obvious decreasing trend with higher water turbidity.

Chapter 4 Underwater Single-Pixel Imaging Quality

4.1 Underwater Single-Pixel Imaging System Setup

The effect of water turbidity and wavelength of laser source are further studied in an underwater single-pixel imaging system that uses a pulse laser as a light source. Figure 12 shows the schematic setup of the underwater single-pixel imaging system. The experimental setup of underwater single-pixel imaging is shown in Figure 13. The experimental setup consists of the photodetector (Thorlabs PDA36A-EC), collecting lens, DMD (DLP Light Crafter 6500 Thorlabs), water tank, transparent target, data acquisition module (DAQ, National Instrument USB-6001DAQ), and laser (532 nm and 635nm laser emitter). The laser emitted on the DMD generates different light illumination patterns onto the target. The portion of the light pattern is transmitted through the transparent object and reaches the photodetectors through a collecting lens to concentrate light intensity at the photodetectors sensor area. The photodetectors are connected to a DAQ to convert the detected signal from analog to digital signal. The digitized signal obtained is essential information for reconstruction using MATLAB software.

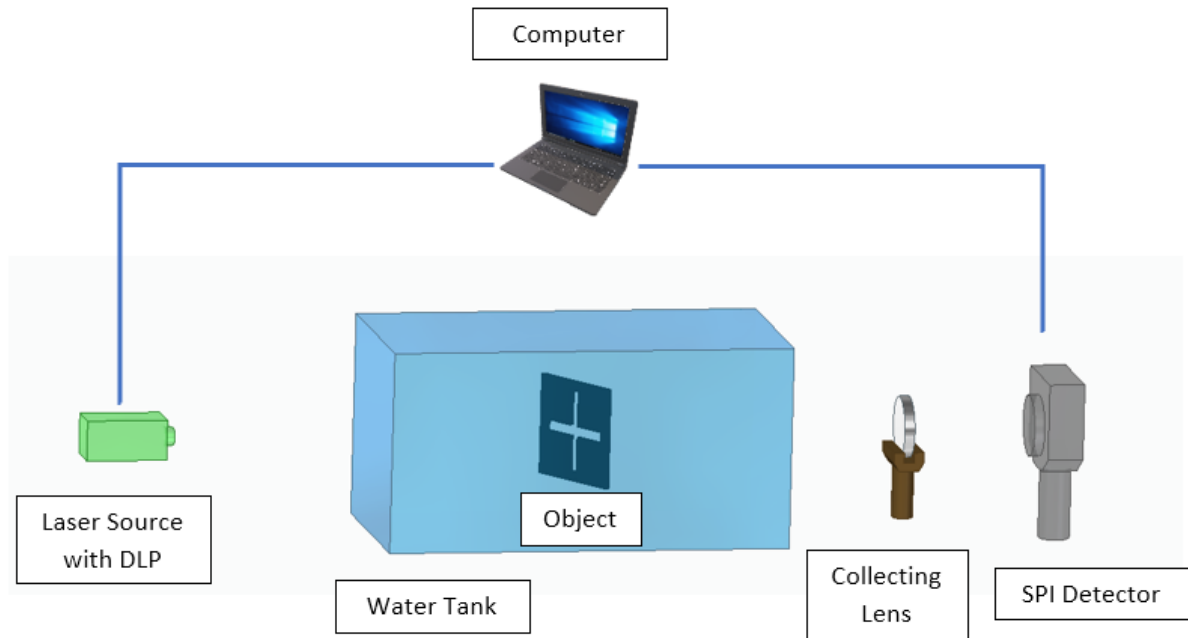


Figure 12 Schematic diagram of underwater single-pixel imaging

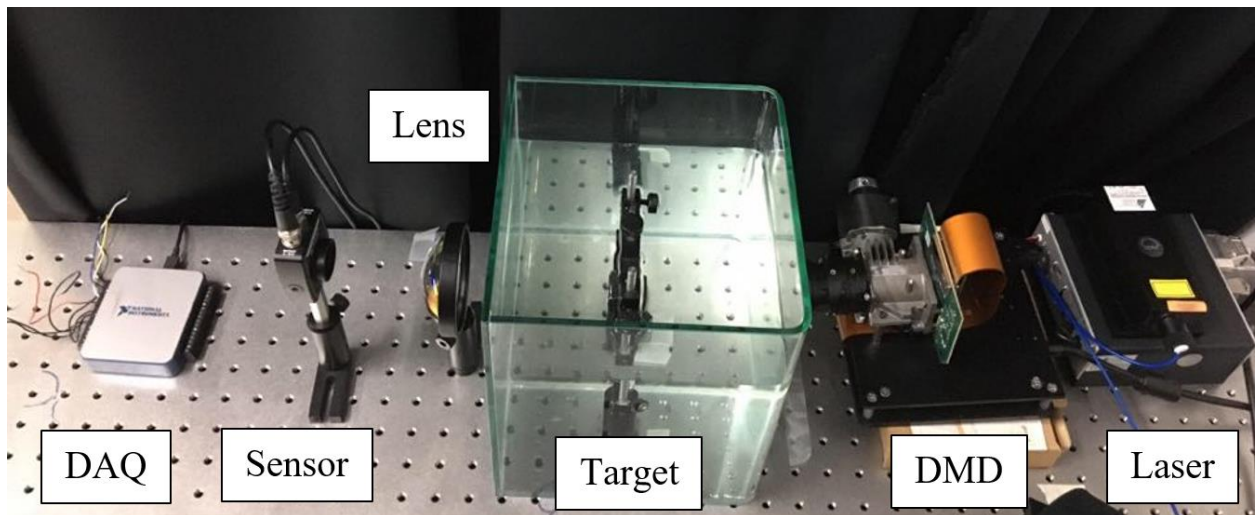


Figure 13 Experimental setup of underwater single-pixel imaging.

4.2 Single-Pixel Imaging Reconstruction via Block Compressive Sensing

4.2.1 Compressive Sensing

4.2.2.1 Conventional Compressive Sensing

Compressive sensing has the advantages of compression and low sampling of sparse signals with insufficient and non-adaptive linear measurements [94-96]. The principle and theory of compressive sensing help in the development of the single-pixel imaging research field. Compressive sensing has two main factors, sparsity and incoherence. The sparsity of the signal can be represented by the non-zero elements in the signal transform domain. Thus, recovery can be achieved even with only 30% measurements, m from a total number of pixels, N [97].

$$Y = \phi X \quad (17)$$

Where ϕ is the sampling operator and Y is the random samples. Then, X is the target to be recovered or reconstructed from Y . ϕ is designed to reconstruct X from Y

$$X = \phi' Y \quad (18)$$

Additional constraints are needed to be applied on signal X to minimize the total sampling measurement required. Let $\{\Psi_i\}_{i=1}^N$ be the orthonormal basis for space R^N . X can be expressed as a linear combination of the basis vectors:

$$X = \sum_{i=1}^n Z_i \Psi_i \quad (19)$$

The coefficients Z_i are evaluated by the products $Z_i = \langle X, \Psi_i \rangle$. Vector X can be simplified with linear regression by:

$$X = \Psi Z \quad (20)$$

where the matrix Ψ is orthogonal with Ψ^T and Z , the vector has $K \ll N$ measurements.

Substituting eq. 20 in eq. 17, we obtain

$$Y = \Phi \Psi Z \quad (21)$$

The recovery of X can be achieved by applying l_1 minimization. The recovery processing time can be shortened when the signal is sparse, which is containing a fewer number of significant coefficients, with the remaining coefficients are zeros. All the audio, image, and video signals are usually sparse on some basis. From Eq. (17), where $\Phi \in C^{m \times N}$, Φ is a sparse matrix that meets RIP, and X is a k -sparse vector that only has k number of the non-zero coefficient. Then, the l_1 minimization model can be expressed by:

$$\min \{ \|X\|_1 : \|\Phi X - Y\|_2 \leq \gamma \} \quad (22)$$

Where γ is the generic norm, $\gamma \geq 0$. Let $Y = \Phi X^\wedge$ where X^\wedge is sparse. $X^\wedge(k)$ would be the closest approximation of X and X^\wedge to be the optimal solution. Then, the recovery outcome is bounded by the sparsity of the measurement matrix, and it can be expressed by the following:

$$\|X^* - X^\wedge\|_2 \leq C k^{\frac{1}{2}} \|X^\wedge - X^\wedge(k)\|_1 \quad (23)$$

$$\|X^* - X^\wedge\|_1 \leq C \|X^\wedge - X^\wedge(k)\|_1 \quad (24)$$

where C is a generic constant, and sparsity k can be set to the order of $m/\log(\frac{n}{m})$ based on the matrix type used. Then, the model with higher stability can be expressed by the following:

$$\|X^* - X^\wedge\|_2 \leq C \left(\gamma + k^{\frac{1}{2}} \|X^\wedge - X^\wedge(k)\|_1 \right) \quad (25)$$

where $\hat{X} = \hat{X}(k)$ and $\gamma = 0$. Then, the exact recovery $X^* = \hat{X}$ can be achieved with the relevant measurement matrix (Φ).

4.2.2.2 Block Compressive Sensing

Conventional compressive sensing is usually utilized for 1-D signals. Thus, images that are in 2-D require converting from 2-D signals to 1-D signals. Solving 1-D long vector signals in conventional compressive sensing has the downside of computational complexity and massive storage for measurement matrix. A codec can be used to compress data for more efficient data transmission, but it is expensive.

The block compressive sensing is one of the solutions for the stated limitations of compressive sensing [98, 99]. In block compressive sensing, it is not required to convert 2-D signals to 1-D signals. Instead, it divides 2-D signal, X into small square blocks with size $\sqrt{n} * \sqrt{n}$. The signal X can be written in terms of block matrix as:

$$X = \begin{bmatrix} X_1 & X_2 & \cdots & X_{\sqrt{L}} \\ X_{\sqrt{L}+1} & X_{\sqrt{L}+2} & \cdots & X_{2\sqrt{L}} \\ \vdots & \vdots & \ddots & \vdots \\ X_{L-\sqrt{L}+1} & X_{L-\sqrt{L}+2} & \cdots & X_L \end{bmatrix} \quad (26)$$

where $L = \frac{N}{n}$ and X_i is the square blocks matrix of signal X with $i = (1,2,3 \dots L)$. To simplify the solving complexity, we always assume L is an integral.

Let K_i to be the sparsity level of X_i with $i = (1,2,3 \dots L)$. Thus, $K_{max} = \|K\|_\infty$ which is the maximum sparsity level in vector K . Let x_i be the vectorized signal with $i = (1,2,3 \dots L)$. Then, the measurement vector of x_i after raster scanning can be obtained with

$$y_i = \Phi_G x_i \quad (27)$$

where $\Phi_G \in \mathbb{C}^{m \times N}$ is a Gaussian random matrix. Similar to conventional compressive sensing, each square block in signal X can be recovered with l_1 minimization if Φ_G meets RIP with order K_{max} .

4.2.2 Image Reconstruction Algorithm via Block Compressive Sensing

Figure 14 shows the flowchart of reconstruction of the single-pixel imaging reconstruction algorithm. The image size of the target object, N which is representing the total resolution or pixels in the image. Then, the number of measurements, m for reconstruction is evaluated from $m = O * (K \log(N))$. The number of measurements, m needed is determined by the sparsity of the binary matrix used. After calculating the number of measurements required, the measurement process runs until the number of detected sample measurements equal to m . After that, the initial guess of signal X can be obtained by l_1 minimization algorithm and X value is updated after every l_1 minimization algorithm iteration. Finally, the reconstructed image can be obtained.

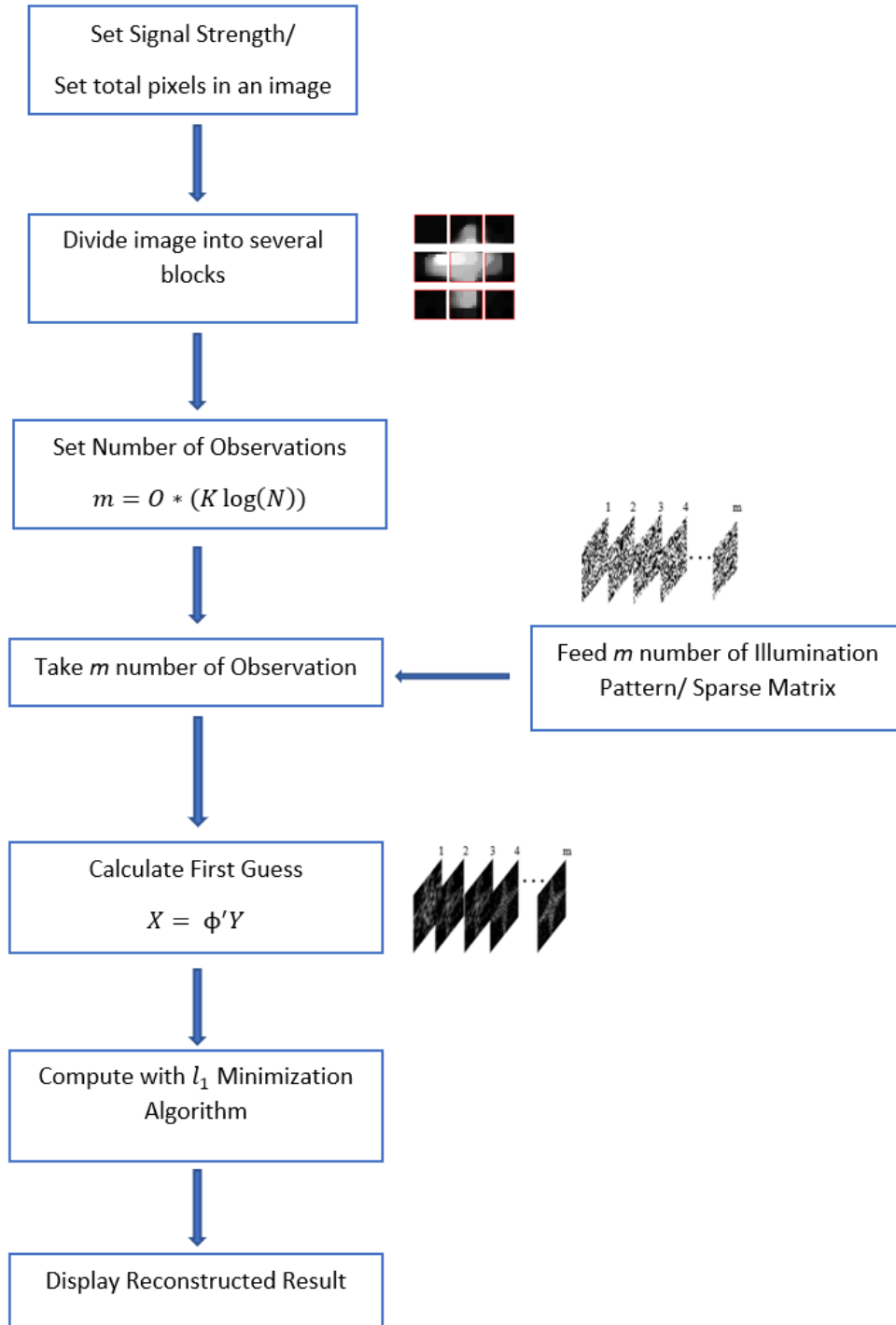


Figure 14 Flowchart of the single-pixel imaging reconstruction algorithm.

4.3 Underwater Single-Pixel Imaging Quality Evaluation

Peak Signal-to-Noise-Ratio (PSNR) and Structural Similarity Index (SSIM) are usually being applied in research studies related to image reconstruction to evaluate the performance of the reconstruction process. Thus, these two methods are being applied in this study to measure and compare the reconstructed image quality. PSNR can be expressed as below:

$$PSNR = 10 * \log_{10} \frac{MAX_1^2}{MSE} \quad (28)$$

where MAX_1^2 is the highest pixel value detected of the image. Since the data are measured in eight bits per pixel, so the maximum possible pixel value that can be obtained is value 255. The MSE in Eq. (28) is the product of the mean and squared difference between the original and the reconstructed image. MSE can be expressed as below:

$$MSE = \frac{1}{mn} * \sum_{i=0}^{m-1} \sum_{j=0}^{n-1} [O(i,j) - R(i,j)]^2 \quad (29)$$

Where mn is the total number of pixels, moreover, $O(i,j)$ and $R(i,j)$ are the original and reconstructed images, respectively.

SSIM is the method to measure the analogy between the images. Basically, SSIM evaluates the deterioration of the image, which is induced due to compression and data destruction operations during transmission. In this study, the computing process is done using MATLAB software to evaluate the SSIM between the original and reconstructed image. The SSIM computing equation between images x and y can be expressed as below:

$$SSIM(x, y) = \frac{(2\mu_x\mu_y + c_1)(2\sigma_{xy} + c_2)}{(\mu_x^2 + \mu_y^2 + c_1)(\sigma_x^2 + \sigma_y^2 + c_2)} \quad (30)$$

$$c_1 = (k_1L)^2 \quad c_2 = (k_2L)^2 \quad \& \quad k_1 = 0.01 \quad k_2 = 0.03$$

Where μ and σ representing average and variance, respectively. σ_{xy} is the covariance of \mathbf{x} and \mathbf{y} . L is the image pixel value range. In general, SSIM is more reliable to measure the deterioration of image quality compared to PSNR because SSIM follows visible structures in the object [63].

4.4 Results and Discussion

4.4.1 The Effect of Image Resolution and Number of Measurements

In this study, images are reconstructed on different total pixels of an image (32 x 32, 64 x 64, and 128 x 128) with the same number of total 64 measurements to compare the impact of image resolution. Although the reconstructed images have the same sampling number, Figure 15 clearly shows that the recovered images have more details at edges in the image with higher resolution.

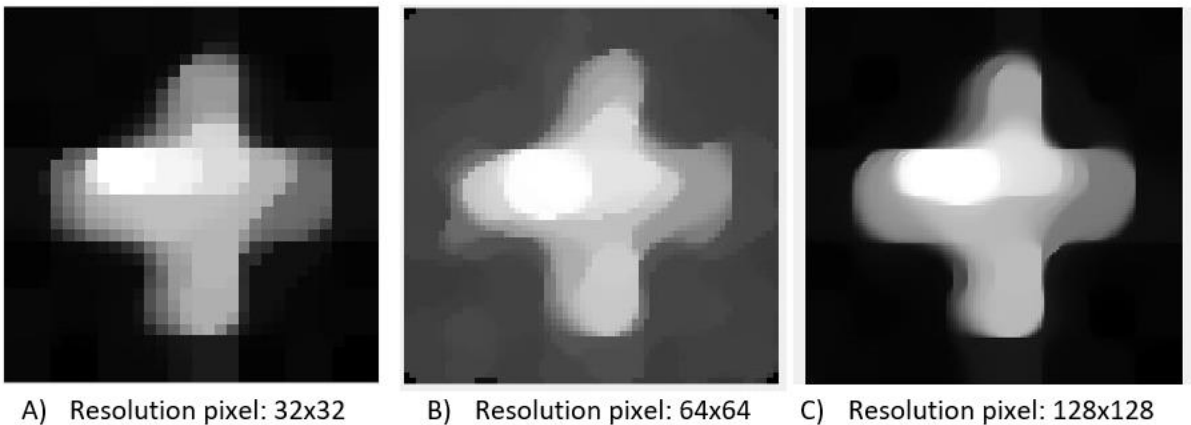


Figure 15 Reconstructed images with the same number of total measurements, 64 measurements.

Moreover, to compare the impact of the total number of measurements in reconstructed images, images also have been reconstructed on a different number of measurements with the same image resolution. By comparing the recovered images in Figure 16, it shows that reconstructed images with a lesser number of measurements tend to have more noise due to insufficient sampling.

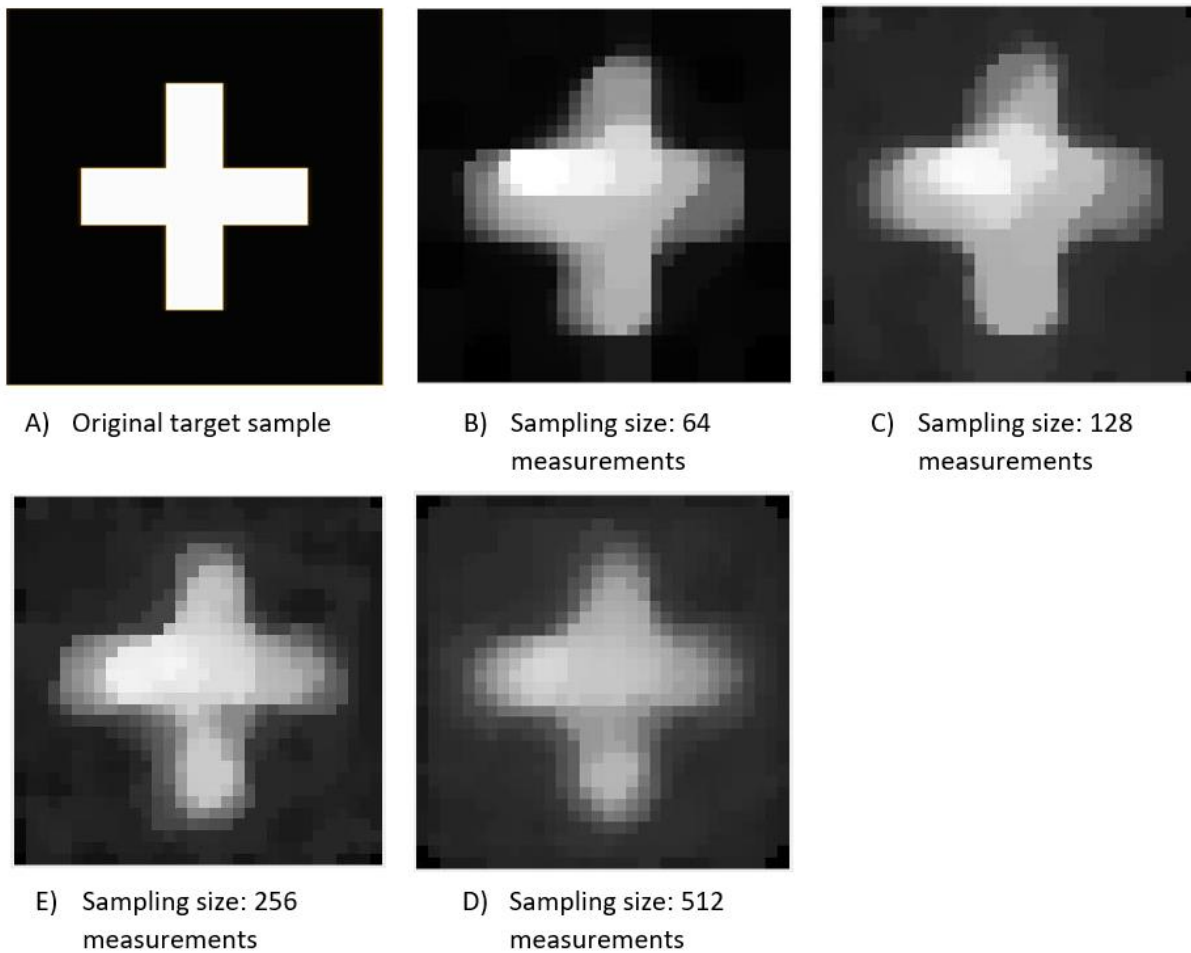


Figure 16 Reconstructed images with a different number of measurements and same resolution level.

Then, the PSNR and SSIM of each recovered image are evaluated and plotted in Figure 17 and Figure 18. The calculated PSNR and SSIM show a proportional ascending trend of PSNR and SSIM with higher resolution reconstructed images. Thus, it shows images with higher resolution have better response and image quality after reconstruction. Figure 17 and Figure 18 indicate that the reconstructed images with higher sampling numbers have a significant upward trend in both PSNR and SSIM calculated. Thus, it shows that reconstruction with a higher sampling number provides a more reliable, better-reconstructed image and performance.

As discussed in section 4.2.1, compressive sensing mainly made up of three operations: sparse representation, measurement, and sparse recovery. Sparse representation is to ensure the signal obtained is sparse to apply compressive sensing. Then, the sufficient number of incoherent measurements, m is required to recover signal image, X . Finally, sparse recovery can be achieved by applying l_1 minimization.

The sufficient number of measurements, m required could be described by:

$$m = K \log N \quad (31)$$

Where N is the total pixel in the original signal and K is the non-zero entries in the column vector of N . Thus, the higher the number of measurements obtained, the model or signal can recover with more complexity.

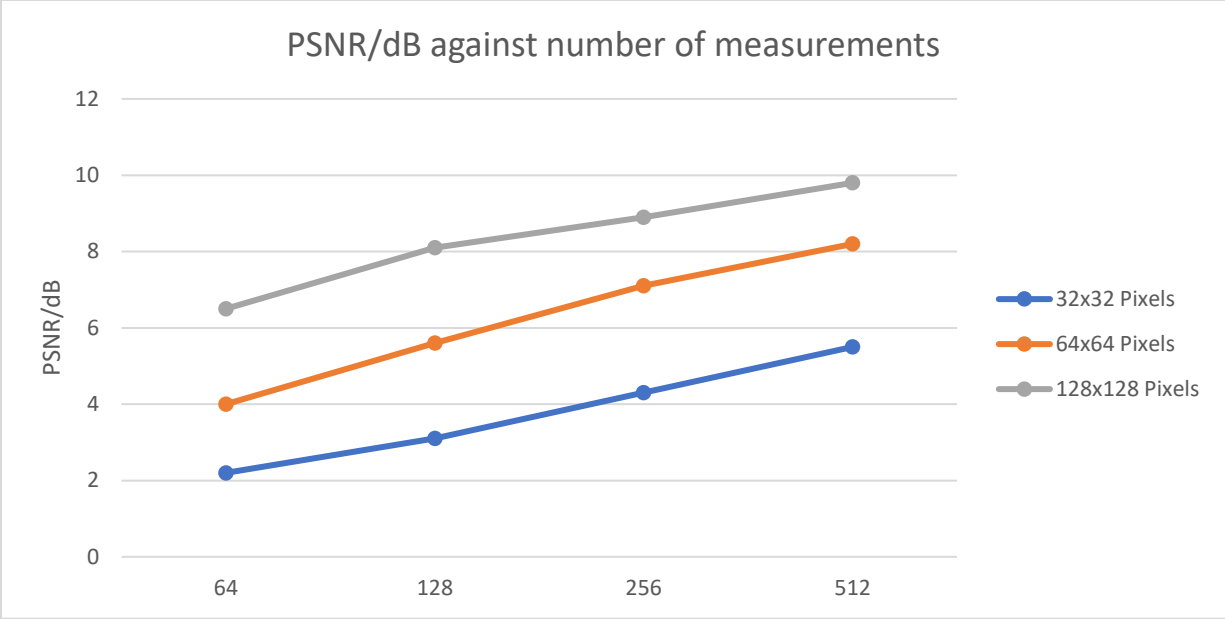


Figure 17 PSNR/dB against the number of measurements of reconstructed images

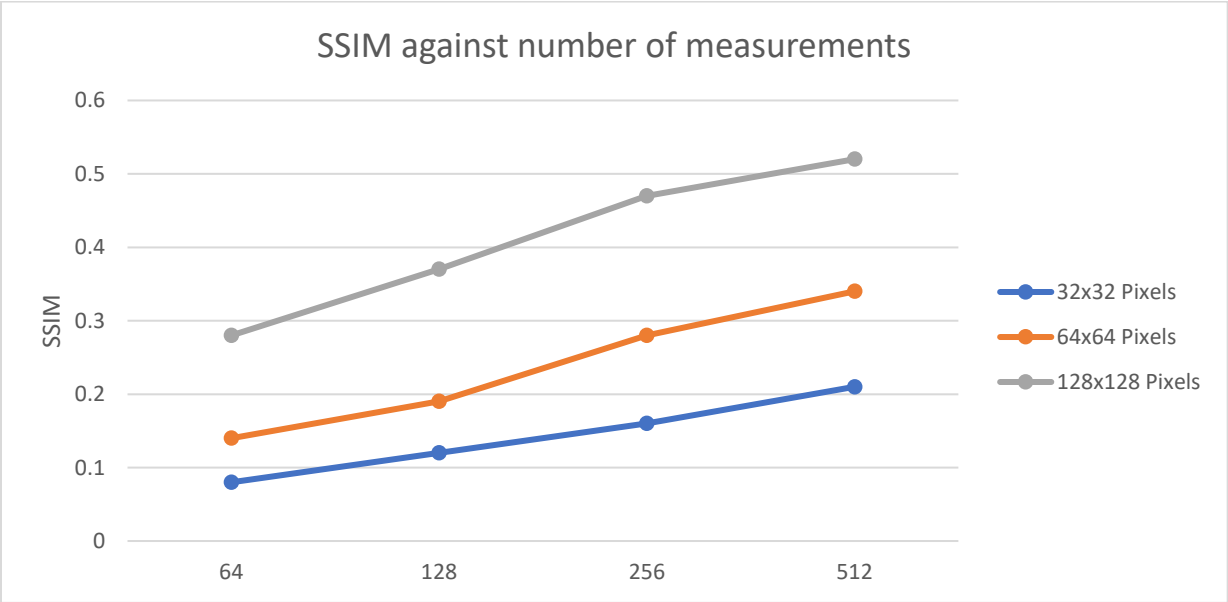
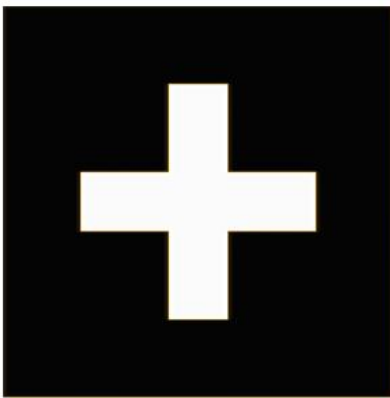


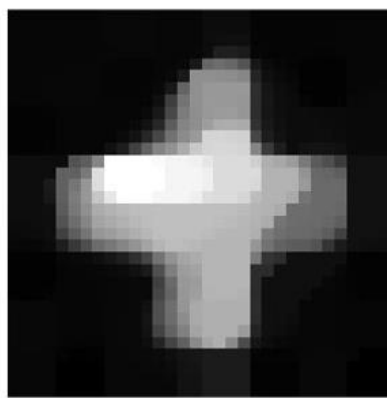
Figure 18 SSIM against the number of measurements of reconstructed images.

4.4.2 The Effect of Water Turbidity Level

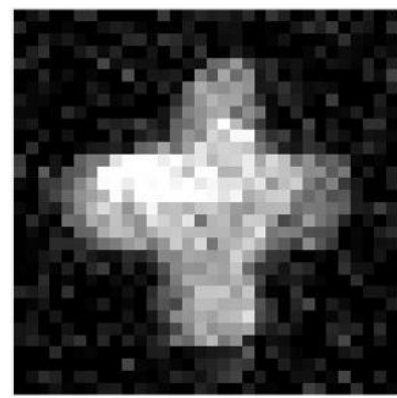
The image reconstruction will be affected by the turbidity level in the water, mainly due to the variations of refractive index in the water, and eventually leads to the variation of detected intensity as discussed in section 0. To further analyze the effect on image reconstruction, several images are reconstructed in different water turbidity levels. From Figure 19, it clearly shows reconstructed images have a higher noise level in higher water turbidity level. At above 100NTU of turbidity level, the reconstructed images show obvious deterioration but remain distinctive on the shape of the target.



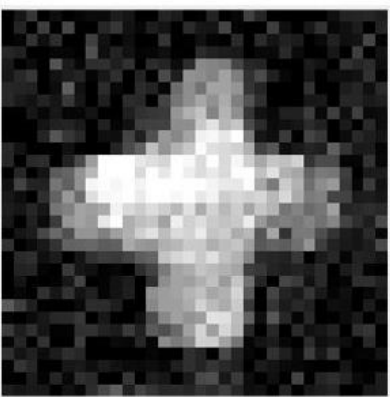
A) Original target sample



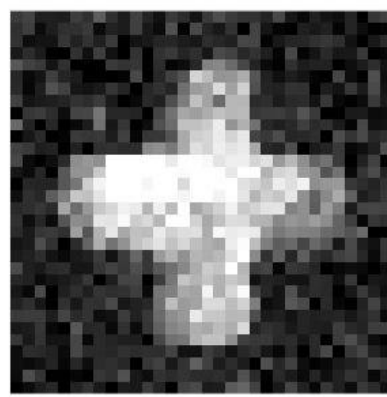
B) Turbidity level: 0 NTU



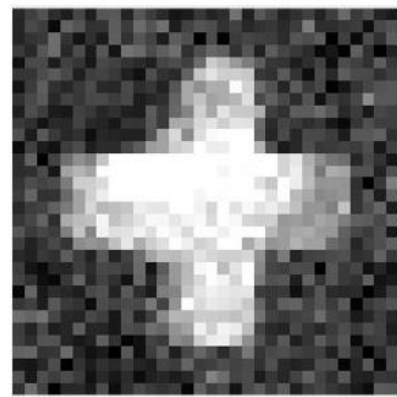
C) Turbidity level: 50 NTU



D) Turbidity level: 100 NTU



E) Turbidity level: 150 NTU



F) Turbidity level: 200 NTU

Figure 19 Reconstructed images on different water turbidity level with the same number of measurements and image resolution

The PSNR and SSIM of recovered images at different turbidity levels are plotted in Figure 20 and Figure 21. The plots show that the PSNR and SSIM didn't reduce much at turbid degrees up to 50NTU but show a significant decreasing trend above 100NTU turbid degrees. Furthermore, the turbidity level's effect could be reduced with higher image resolution, as shown in the plots.

The image quality reducing in a higher turbid degree medium is mainly due to the scattering and absorption effect. Scattering is a minimum of spectrally dependent, and it causes variation on the angle of the photon transmission path. Absorption is spectrally dependent and will directly remove the photons from the transmission path permanently. The medium, concentration, and composition of the particulates define the medium's coefficient magnitude and spectral features. As inherent optical properties (IOPs) are conservative properties, the medium's absorption coefficient varies linearly with absorbing particulates' concentration and composition [100]. Thus, the attenuation coefficient of the medium increases as the concentration of the absorbing particulates increases. This causes the lesser reflected light intensity to be detected by the receiver and eventually affects overall system performance. Moreover, the high turbid degree medium causes high sparsity in the reflected signal as well. This eventually affects the reconstruction quality of the images.

As discussed in section 3.3.3, the impact factor of intensity error decreases with a higher attenuation coefficient. Thus, the higher the turbidity level in the water, the higher the attenuation coefficient, and the lesser the returned laser power. In other words, the higher turbidity level in the water causes lesser the reflected laser power in the medium and leads to a decrease in image quality after reconstruction. This shows the reconstruction also heavily relies on the reflected intensity for better performance in image reconstruction.

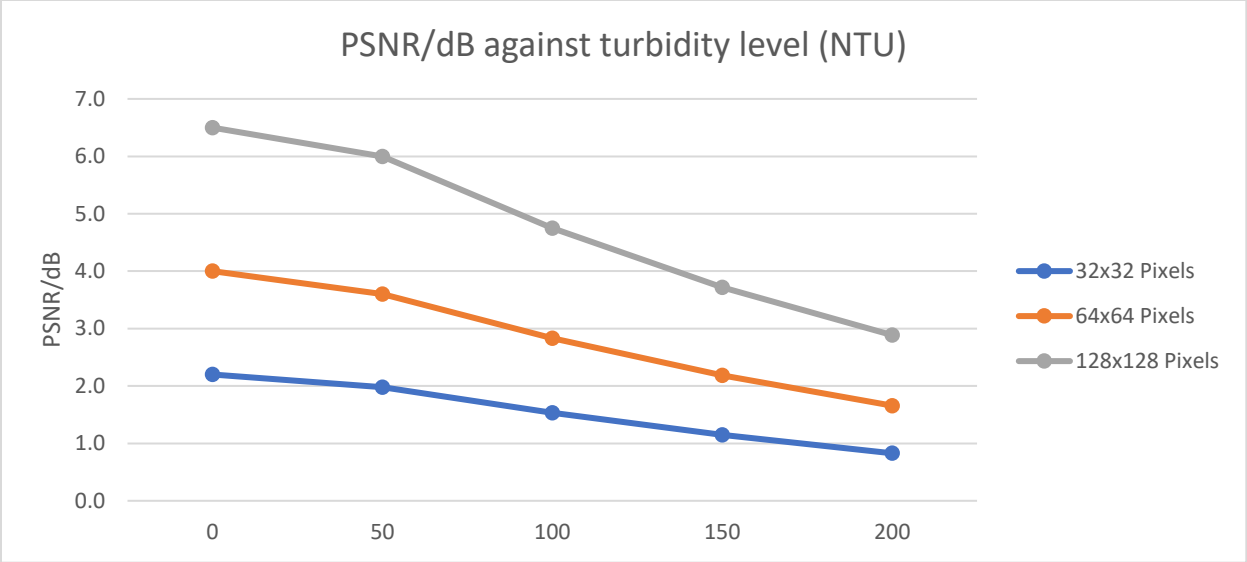


Figure 20 PSNR/dB against turbidity level (NTU) with the same number of measurements.

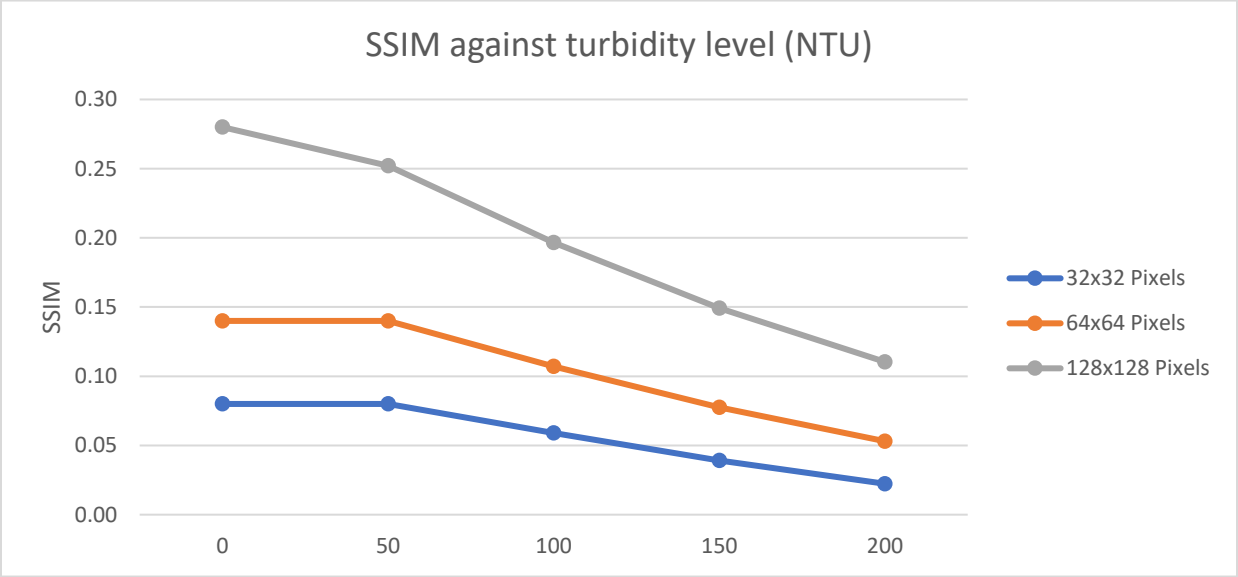


Figure 21 SSIM against water turbidity level (NTU) with the same number of measurements.

4.4.3 The Effect of Laser Source Wavelength

To compare the performance of reconstruction with different laser source wavelengths, red (635nm) and green (532nm) laser sources are used in this study. Thus, in Figure 22 and Figure 23, several images are reconstructed with different water turbidity levels and laser sources. By comparing the reconstructed images, it clearly shows that the reconstruction with a longer wavelength laser source, red laser, has better reconstruction quality and performance in underwater imaging. Image reconstructed with shorter wavelength laser source, green laser, shows more noise, lesser details around target edges and less distinctive on target at high turbid degrees.

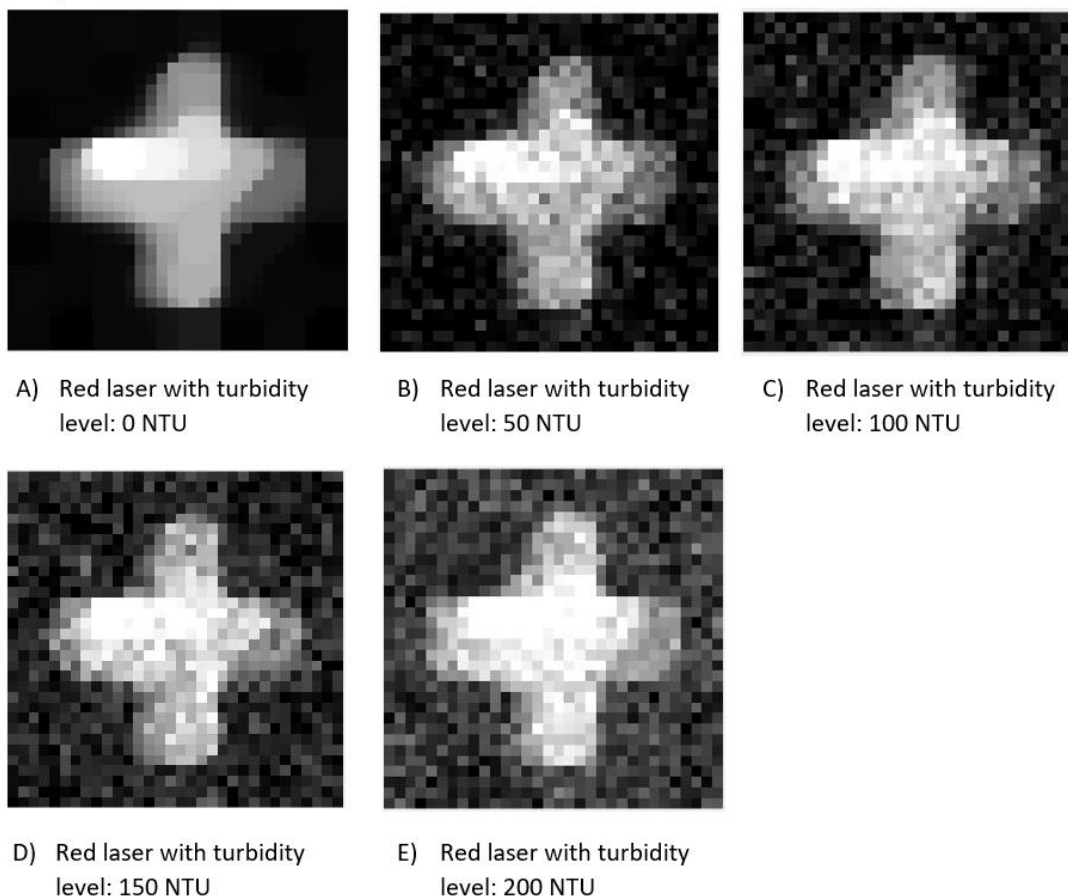


Figure 22 Reconstructed images with different water turbidity levels in red laser source.

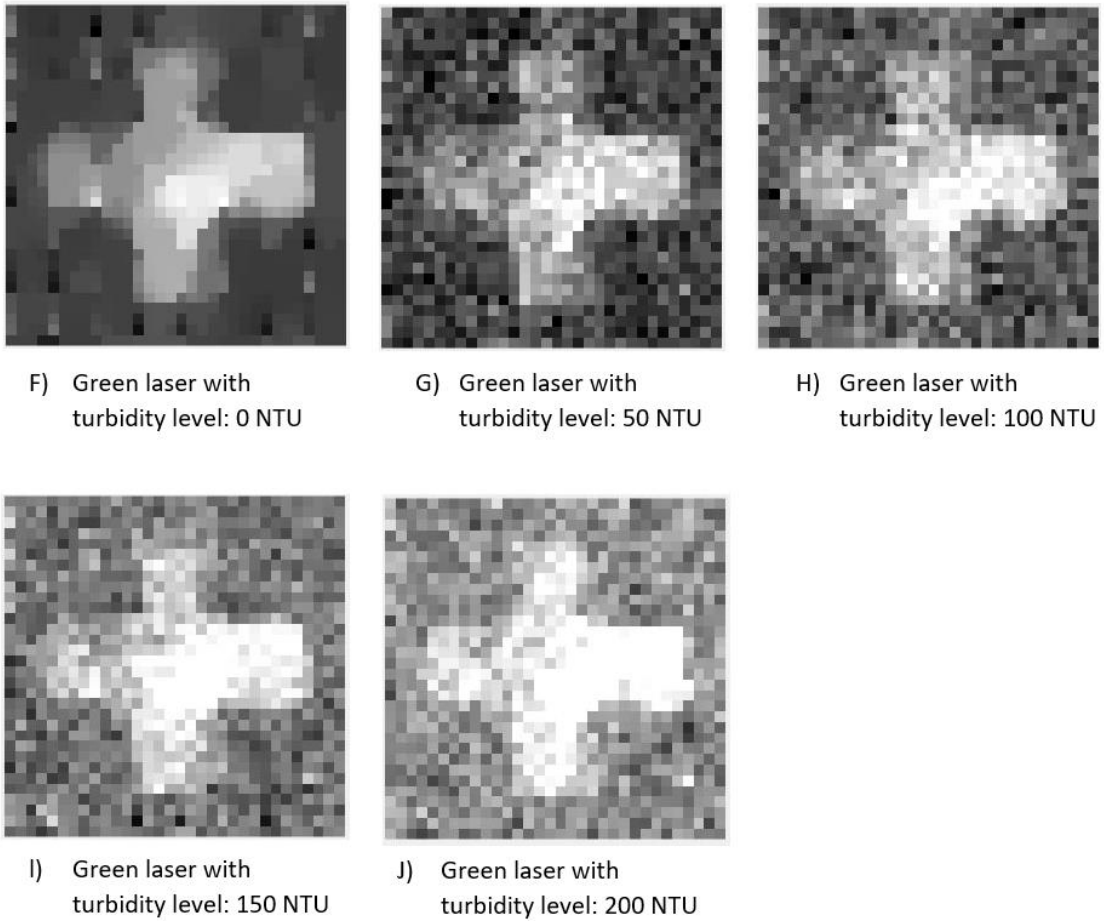


Figure 23 Reconstructed images with different water turbidity levels by comparison in red and green laser source.

The PSNR and SSIM of recovered images are compiled in Figure 24 and Figure 25. It shows the reconstructed quality with a shorter wavelength laser source, green laser, has a similar trend as the red laser. Overall, the PSNR and SSIM of reconstruction with a shorter wavelength laser source, green laser, is significantly lesser. This is mainly due to the higher wavelength laser source has a lesser refractive index in underwater medium and leads to lesser variation in detected light intensity by the sensor.

Refraction of light occurs when light is transmitted through refractive mediums. The refractive index varies with the wavelength of light linearly due to different wavelengths that interfere with the molecules of the medium to different extents. The relationship between the refractivity of light and the wavelength is described as below:

$$\mu = \frac{c}{v} \quad (32)$$

where μ is the refractive index. c and v are the speed of light in the vacuum and medium, respectively. Different wavelength of light has different speed of light, and it can be described as below:

$$v = f * \lambda \quad (33)$$

where f and λ are frequency and wavelength of light. Red light travels faster among the visible light spectrum due to its longer wavelength and lower frequency. As red light has a longer wavelength and faster travel speed, red light has a lower refractive index among the visible light spectrum. This causes more light detected at the sensor in the underwater imaging system and giving better quality and performance in image reconstruction. Moreover, the high turbid degree medium causes high sparsity in the reflected signal as well. This eventually affects the reconstruction quality of the images.

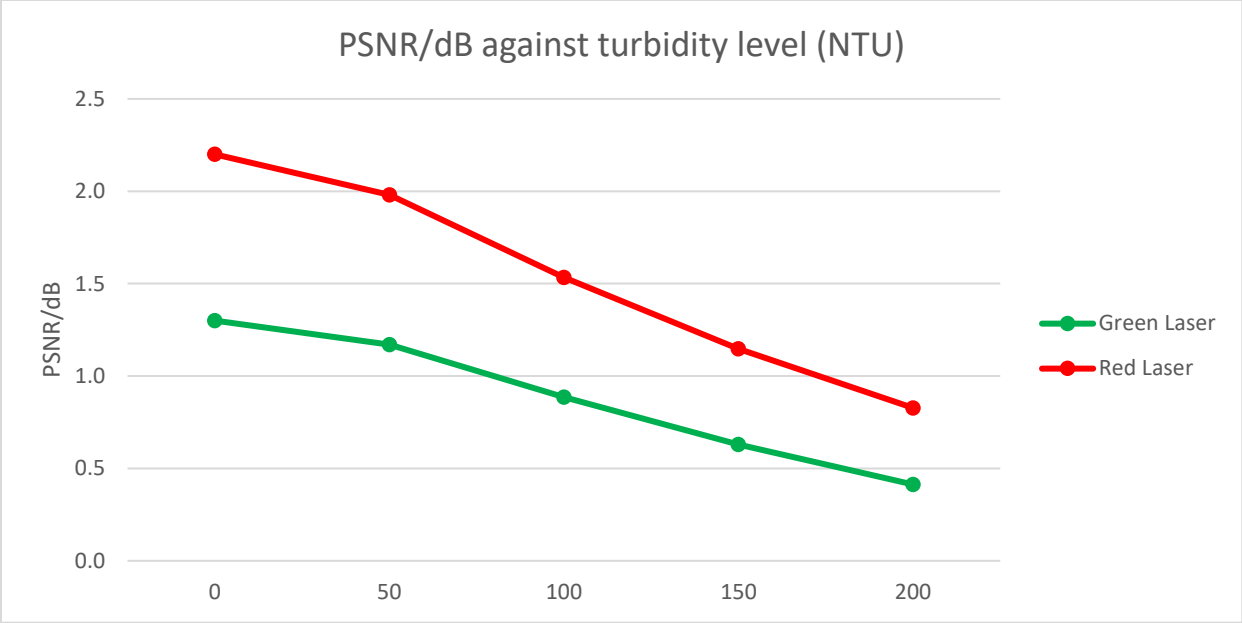


Figure 24 PSNR/dB against turbidity level (NTU) by comparison in red and green laser source.

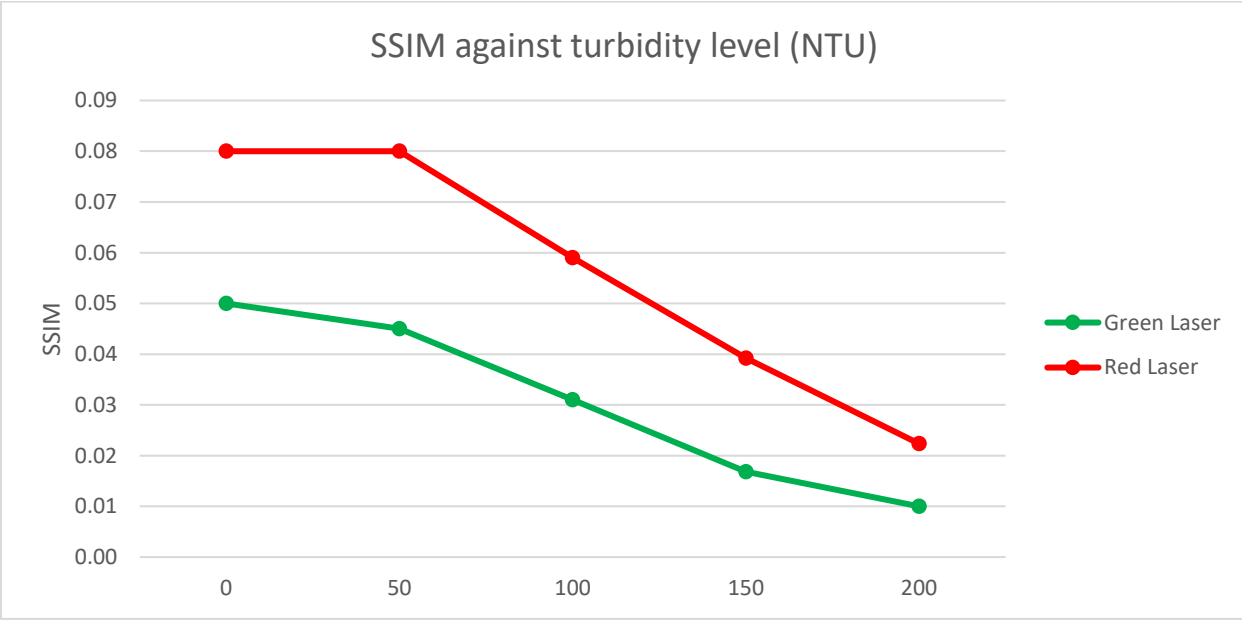


Figure 25 SSIM against turbidity level (NTU) by comparison in red and green laser source.

Chapter 5 Conclusion

5.1 Summary of Findings

Different factors in underwater imaging are investigated in this study, including the effect of water turbulence, salinity, and turbidity. The experimental results are analyzed based on reflection ratio and range error accuracy. The experimental results show that the reflection ratio has an inversely proportional trend with water turbulence, salinity, and turbidity effects. Among the three factors, the reflection ratio of reflected intensity shows the most considerable reduction in the water turbidity effect. Moreover, the range error shows consistent and no significant variations with the increase of water turbulence and salinity. However, the range error shows an obvious decreasing trend with higher water turbidity. This is mainly due to the significant absorption effect in higher water turbidity levels compared to other factors.

Thus, the influence of water turbidity on the quality of single-pixel imaging is further investigated. In this study, the image quality of reconstructed single-pixel imaging is analyzed in terms of PSNR and SSIM. The experimental results show that the image quality decreases with a higher turbidity level. This is mainly due to higher refraction and absorption in a medium with high turbid degrees.

Furthermore, several variables of single-pixel imaging are investigated, including the resolution, number of measurements, and wavelength of the laser source. The experimental results show that the higher the image resolution, the higher the reconstructed image quality. It shows more details around the edges at a higher resolution image because a lower resolution image shows blurred out at the edges of an object. Moreover, the higher the number of measurements or sampling rate provides higher image quality after reconstruction. With the block compressive

sensing technique, the shape of the target is identifiable and distinctive even at a low sampling rate, 64 total measurements. Last but not least, experimental results with different wavelengths of the laser source (green laser, 532nm, and red laser 635nm) are being compared and analyzed. As a higher wavelength laser has lesser refraction in transmission, the underwater image quality after reconstruction with red laser shows better reconstruction quality than green laser.

In conclusion, underwater single-pixel imaging is usually affected by various factors in the actual underwater situation. The use of block compressive sensing technique in underwater single-pixel imaging shows convincing performance even at a low sampling rate. To reduce the refraction factors in underwater single-pixel imaging where it is more critical in being affected by refraction, a higher wavelength laser source shows lower refraction characteristics and could improve the underwater imaging performance.

5.2 Future Work

In this study, underwater single-pixel imaging has been investigated, and results have shown that it is an effective and efficient method. However, more studies and researches would need to be done to improve the overall imaging system performance and quality. In recent years, artificial intelligence and machine learning are popular among researchers to enhance system performance further. Deep learning and convolutional neural network are machine learning methods that can analyze visual imagery. Deep learning in the imaging system has been researched widely, especially in the medical field [101-104]. It has shown that it can improve medical imaging systems' efficiency and quality, such as chest computed tomography (CT) scans. Thus, it is also recommended to apply deep learning in underwater single-pixel imaging to enhance the overall imaging quality.

References

- [1] M.-C. Amann, T. M. Bosch, M. Lescure, R. A. Myllylae, and M. Rioux, "Laser ranging: a critical review of unusual techniques for distance measurement," 2001, vol. 40: SPIE, p. 10.
- [2] J. Lee, K. Lee, S. Lee, S.-W. Kim, and Y.-J. Kim, "High precision laser ranging by time-of-flight measurement of femtosecond pulses," *Measurement Science and Technology*, vol. 23, no. 6, p. 065203, 2012, doi: 10.1088/0957-0233/23/6/065203.
- [3] L. Xiuhua, W. Wenfu, G. Junrong, and S. Liming, "The Method and Development Trend of Laser Ranging," vol. 2, ed, 2013, pp. 7-10.
- [4] P. Andersson, "Long-range three-dimensional imaging using range-gated laser radar images," 2006, vol. 45: SPIE, p. 10.
- [5] E. Baumann, F. R. Giorgetta, J. D. Deschênes, W. C. Swann, I. Coddington, and N. R. Newbury, "Comb-calibrated laser ranging for three-dimensional surface profiling with micrometer-level precision at a distance," *Optics express*, vol. 22, no. 21, p. 24914, 2014, doi: 10.1364/OE.22.024914.
- [6] L. Dan, S. Jian-Feng, L. Qi, and W. Qi, "Model-based recognition of 3D articulated target using lidar range data.(Report)(Author abstract)," vol. 54, no. 17, p. 5382, 2015, doi: 10.1364/AO.54.005382.
- [7] A. McCarthy, R. J. Collins, N. J. Krichel, V. Fernandez, A. M. Wallace, and G. S. Buller, "Long-range time-of-flight scanning sensor based on high-speed time-correlated single-photon counting," *Applied Optics*, vol. 48, no. 32, 2009, doi: 10.1364/AO.48.006241.
- [8] G. Chingseong Tan, A. Seet, A. Sluzek, and A. Shacklock, "Three-dimensional Machine Vision Using Gated Imaging System: A Numerical Analysis," ed, 2006, pp. 1-6.
- [9] B. Höfle and N. Pfeifer, "Correction of laser scanning intensity data: Data and model-driven approaches," *ISPRS Journal of Photogrammetry and Remote Sensing*, vol. 62, no. 6, pp. 415-433, 2007, doi: 10.1016/j.isprsjprs.2007.05.008.
- [10] Y. Bi, X. Xu, S. Y. Chua, E. M. T. Chow, and X. Wang, "Underwater Turbulence Detection Using Gated Wavefront Sensing Technique," *Sensors (Basel, Switzerland)*, vol. 18, no. 3, 2018, doi: 10.3390/s18030798.
- [11] Z. Chen, Z. Zhang, F. Dai, Y. Bu, and H. Wang, "Monocular Vision-Based Underwater Object Detection," *Sensors (Basel, Switzerland)*, vol. 17, no. 8, 2017, doi: 10.3390/s17081784.
- [12] R. Lueck, F. Wolk, and H. Yamazaki, "Oceanic Velocity Microstructure Measurements in the 20th Century," edited by *The Oceanographic Society of Japan*, vol. 58, no. 1, pp. 153-174, 2002, doi: 10.1023/A:1015837020019.
- [13] W. Ma, *Design and Sea Trials of the Underwater Glider for Micro-structure Turbulence Measurement*. 2017, p. 022.
- [14] B. Ouyang et al., *Compressive line sensing underwater imaging system* (no. 5). SPIE, 2014, pp. 1-16, 16.
- [15] M. Li, A. Mathai, S. L. H. Lau, J. W. Yam, X. Xu, and X. Wang, "Underwater Object Detection and Reconstruction Based on Active Single-Pixel Imaging and Super-Resolution Convolutional Neural Network," *Sensors (Basel)*, vol. 21, no. 1, p. 313, 2021, doi: 10.3390/s21010313.
- [16] Q. Chen, J. W. Yam, S. Y. Chua, N. Guo, and X. Wang, "Characterizing the performance impacts of target surface on underwater pulse laser ranging system," *Journal of quantitative spectroscopy & radiative transfer*, vol. 255, p. 107267, 2020, doi: 10.1016/j.jqsrt.2020.107267.
- [17] X. Wang et al., "Underwater three-dimensional range-gated laser imaging based on triangular-range-intensity profile spatial-correlation method," vol. 10020, ed, 2016, pp. 1002006-1002006-6.

- [18] B. Fu, K. Yang, J. Rao, and M. Xia, "Analysis of MCP gain selection for underwater range-gated imaging applications based on ICCD," *Journal of Modern Optics*, vol. 57, no. 5, pp. 408-417, 2010, doi: 10.1080/09500341003678772.
- [19] X. Wang, L. Hu, Q. Zhi, Z.-Y. Chen, and W.-Q. Jin, "Influence of range-gated intensifiers on underwater imaging system SNR," vol. 8912, ed, 2013, pp. 89120E-89120E-8.
- [20] S. Y. Chua, X. Wang, N. Guo, and C. S. Tan, "Influence of target reflection on three-dimensional range gated reconstruction," *Applied Optics*, vol. 55, no. 24, pp. 6588-6595, 2016/08/20 2016, doi: 10.1364/AO.55.006588.
- [21] C. Sing Yee, W. Xin, G. Ningqun, and T. Ching Seong, "Range compensation for accurate 3D imaging system.(Report)(Author abstract)," vol. 55, no. 1, p. 153, 2016, doi: 10.1364/AO.55.000153.
- [22] M. Laurenzis, F. Christnacher, D. Monnin, and I. Zielenski, "3D range-gated imaging in scattering environments," vol. 7684, ed, 2010, p. <xocs:firstpage xmlns:xocs="" />.
- [23] L. Bartolini *et al.*, "Underwater three-dimensional imaging with an amplitude-modulated laser radar at a 405 nm wavelength," *Applied optics*, vol. 44, no. 33, p. 7130, 2005, doi: 10.1364/AO.44.007130.
- [24] M. Kelly, S. Avramov-Zamurovic, and C. Nelson, *Exploration of multiple wavelength laser beams propagating underwater* (SPIE Defense + Security). SPIE, 2018.
- [25] H. R. Gordon, "Can the Lambert - Beer law be applied to the diffuse attenuation coefficient of ocean water?," *Limnology and Oceanography*, vol. 34, no. 8, pp. 1389-1409, 1989, doi: 10.4319/lo.1989.34.8.1389.
- [26] R. M. Pope and E. S. Fry, "Integrating cavity measurements.(Absorption Spectrum (380-700 nm) of Pure Water, part 2)," *Applied Optics*, vol. 36, no. 33, p. 8710, 1997.
- [27] W. a. Hou, p. Society of Photo-optical Instrumentation Engineers, Ed. *Ocean sensing and monitoring : optics and other methods*. Bellingham, Washington 1000 20th St. Bellingham WA 98225-6705 USA : SPIE Press, 2013.
- [28] B. Zheng, N. Wang, H. Zheng, Z. Yu, and J. Wang, "Object extraction from underwater images through logical stochastic resonance," *Optics letters*, vol. 41, no. 21, p. 4967, 2016, doi: 10.1364/OL.41.004967.
- [29] A. Sluzek and T. C. Seong, *Image Formation in Highly Turbid Media by Adaptive Fusion of Gated Images*. Berlin, Heidelberg: Berlin, Heidelberg: Springer Berlin Heidelberg, 2005, pp. 194-201.
- [30] H. Lu, Y. Li, S. Nakashima, and S. Serikawa, "Turbidity Underwater Image Restoration Using Spectral Properties and Light Compensation," *IEICE Transactions on Information and Systems*, vol. E99.D, no. 1, pp. 219-227, 2016, doi: 10.1587/transinf.2014EDP7405.
- [31] W. Lu, L. Liu, and J. Sun, "Influence of temperature and salinity fluctuations on propagation behaviour of partially coherent beams in oceanic turbulence," *Journal of Optics A: Pure and Applied Optics*, vol. 8, no. 12, pp. 1052-1058, 2006/11/01 2006, doi: 10.1088/1464-4258/8/12/004.
- [32] X. Zhao, Y. Peng, C. Zhai, X. Han, and Y. Zhang, "Influence of Inorganic Salts on the Refraction Index of Water," *Applied Mechanics and Materials*, vol. 716-717, no. Mechanical Engineering and Materials Science, pp. 118-121, 2014, doi: 10.4028/www.scientific.net/AMM.716-717.118.
- [33] X. Zhang, L. Hu, and M.-X. He, "Scattering by pure seawater: effect of salinity," *Optics express*, vol. 17, no. 7, p. 5698, 2009, doi: 10.1364/OE.17.005698.
- [34] W. Hou, S. Woods, E. Jarosz, W. Goode, and A. Weidemann, "Optical turbulence on underwater image degradation in natural environments," *Applied Optics*, vol. 51, no. 14, pp. 2678-2686, 2012/05/10 2012, doi: 10.1364/AO.51.002678.
- [35] F. Hanson and M. Lasher, "Effects of underwater turbulence on laser beam propagation and coupling into single-mode optical fiber," *Applied Optics*, vol. 49, no. 16, pp. 3224-3230, 2010/06/01 2010, doi: 10.1364/AO.49.003224.

- [36] M. H. Mahdieh, "Numerical approach to laser beam propagation through turbulent atmosphere and evaluation of beam quality factor," *Optics Communications*, vol. 281, no. 13, pp. 3395-3402, 2008, doi: 10.1016/j.optcom.2008.02.040.
- [37] N. Farwell, "Optical beam propagation in oceanic turbulence," O. Korotkova, S. Avramov-Zamurovic, H. Gordon, W. Hou, and K. Voss, Eds., ed: ProQuest Dissertations Publishing, 2014.
- [38] Y. Zhang, X. L. Ji, X. Li, and H. Yu, "Thermal blooming effect of laser beams propagating through seawater," *Opt. Express*, vol. 25, no. 6, pp. 5861-5875, 2017, doi: 10.1364/OE.25.005861.
- [39] D. P. Juyal, *Laser Sources for Underwater Applications*. 1983, pp. 57-70.
- [40] G. L. Clarke and H. R. James, "Laboratory Analysis of the Selective Absorption of Light by Sea Water*," *J. Opt. Soc. Am.*, vol. 29, no. 2, pp. 43-55, 1939/02/01 1939, doi: 10.1364/JOSA.29.000043.
- [41] S. A. Sullivan, "Experimental Study of the Absorption in Distilled Water, Artificial Sea Water, and Heavy Water in the Visible Region of the Spectrum*," *J. Opt. Soc. Am.*, vol. 53, no. 8, pp. 962-968, 1963/08/01 1963, doi: 10.1364/JOSA.53.000962.
- [42] N. Wang, H. Zheng, and B. Zheng, "Underwater Image Restoration via Maximum Attenuation Identification," *IEEE Access*, vol. 5, pp. 18941-18952, 2017, doi: 10.1109/ACCESS.2017.2753796.
- [43] F. M. Caimi, D. M. Kocak, F. Dagleish, and J. Watson, "Underwater imaging and optics: Recent advances," ed, 2008, pp. 1-9.
- [44] J. Busck, "Underwater 3-D optical imaging with a gated viewing laser radar," *Optical Engineering*, vol. 44, no. 11, pp. 116001-116007, 2005, doi: 10.1117/1.2127895.
- [45] P. Andersson, "Long-range three-dimensional imaging using range-gated laser radar images," *Optical Engineering*, vol. 45, no. 3, pp. 034301-0343010, 2006, doi: 10.1117/1.2183668.
- [46] D. Letalick *et al.*, "3-D Imaging by Laser Radar and Applications in Preventing and Combating Crime and Terrorism," p. 48, 10/25 2004.
- [47] O. K. Steinvall, H. Olsson, G. Bolander, C. A. Groenwall, and D. Letalick, "Gated viewing for target detection and target recognition," vol. 3707, ed, 1999, pp. 432-448.
- [48] O. Steinvall, P. Andersson, and M. Elmquist, "Image quality for range-gated systems during different ranges atmospheric conditions," vol. 6396, ed, 2006, pp. 639607-639607-17.
- [49] F. Caimi and F. Dagleish, "Performance considerations for continuous-wave and pulsed laser line scan (LLS) imaging systems," *J. Europ. Opt. Soc. Rap. Public.*, vol. 5, p. 10020s, 04/27 2010, doi: 10.2971/jeos.2010.10020s.
- [50] T. E. Giddings, J. J. Shirron, and A. Tirat-Gefen, "EODES-3: an electro-optic imaging and performance prediction model," in *Proceedings of OCEANS 2005 MTS/IEEE*, 17-23 Sept. 2005 2005, pp. 1380-1387 Vol. 2, doi: 10.1109/OCEANS.2005.1639947.
- [51] F. M. Caimi, F. R. Dagleish, T. E. Giddings, J. J. Shirron, C. Mazel, and C. Kophu, "Pulse versus CW Laser Line Scan Imaging Detection Methods: Simulation Results," ed, 2007, pp. 1-4.
- [52] S. G. Narasimhan, S. K. Nayar, S. Bo, and S. J. Koppal, "Structured light in scattering media," vol. 1, ed, 2005, pp. 420-427 Vol. 1.
- [53] M. Levoy, B. Chen, V. Vaish, M. Horowitz, I. McDowall, and M. Bolas, "Synthetic aperture confocal imaging," *ACM Transactions on Graphics (TOG)*, vol. 23, no. 3, pp. 825-834, 2004, doi: 10.1145/1015706.1015806.
- [54] S. Zhang, "Recent progresses on real-time 3D shape measurement using digital fringe projection techniques," *Optics and Lasers in Engineering*, vol. 48, no. 2, pp. 149-158, 2010, doi: 10.1016/j.optlaseng.2009.03.008.
- [55] M. Edgar, G. Gibson, and M. Padgett, "Principles and prospects for single-pixel imaging," *Nature Photonics*, vol. 13, no. 1, pp. 13-20, 2019, doi: 10.1038/s41566-018-0300-7.
- [56] Y. Bromberg, O. Katz, and Y. Silberberg, "Ghost imaging with a single detector," *arXiv.org*, vol. 79, no. 5, 2008, doi: 10.1103/PhysRevA.79.053840.

- [57] M. F. Duarte *et al.*, "Single-pixel imaging via compressive sampling," *IEEE Signal Processing Magazine*, vol. 25, no. 2, pp. 83-91, 2008, doi: 10.1109/MSP.2007.914730.
- [58] S. Ming-Jie and Z. Jia-Min, "Single-Pixel Imaging and Its Application in Three-Dimensional Reconstruction: A Brief Review," *Sensors*, vol. 19, no. 3, 2019, doi: 10.3390/s19030732.
- [59] Y.-Q. Cai, W.-L. Chen, and F. Yuan, "Underwater acoustic image compressive sensing algorithm research based on Bandelets transform," ed, 2016, pp. 1-5.
- [60] B. Ouyang *et al.*, "Underwater laser serial imaging using compressive sensing and digital mirror device," vol. 8037, ed, 2011, pp. 803707-803707-11.
- [61] B. Ouyang *et al.*, *Compressive sensing underwater laser serial imaging system* (no. 2). SPIE, 2013, pp. 1-17, 17.
- [62] Q. Chen, A. Mathai, X. Xu, and X. Wang, "A Study into the Effects of Factors Influencing an Underwater, Single-Pixel Imaging System's Performance," *Photonics*, vol. 6, no. 4, p. 123, 2019, doi: 10.3390/photonics6040123.
- [63] Q. Chen, S. K. Chamoli, P. Yin, X. Wang, and X. Xu, "Active mode single pixel imaging in the highly turbid water environment using compressive sensing," *IEEE Access*, vol. 7, pp. 1-1, 2019, doi: 10.1109/ACCESS.2019.2950896.
- [64] K. Czajkowski, A. Pastuszczak, and R. Kotyński, "Single-pixel imaging with Morlet wavelet correlated random patterns," *Sci Rep*, vol. 8, no. 1, pp. 466-466, 2018, doi: 10.1038/s41598-017-18968-6.
- [65] F. Rousset, N. Ducros, A. Farina, G. Valentini, C. D'Andrea, and F. Peyrin, "Adaptive Basis Scan by Wavelet Prediction for Single-Pixel Imaging," *IEEE Transactions on Computational Imaging*, vol. 3, no. 1, pp. 36-46, 2017, doi: 10.1109/TCI.2016.2637079.
- [66] M.-J. Sun, M. P. Edgar, D. B. Phillips, G. M. Gibson, and M. J. Padgett, "Improving the signal-to-noise ratio of single-pixel imaging using digital microscanning," *Optics express*, vol. 24, no. 10, p. 10476, 2016, doi: 10.1364/OE.24.010476.
- [67] L. Wang and S. Zhao, "Fast reconstructed and high-quality ghost imaging with fast Walsh-Hadamard transform," *Photonics Research*, vol. 4, no. 6, p. 240, 2016, doi: 10.1364/PRJ.4.000240.
- [68] K. Czajkowski, A. Pastuszczak, and R. Kotynski, "Real-time single-pixel video imaging with Fourier domain regularization," *arXiv.org*, vol. 26, no. 16, 2018, doi: 10.1364/OE.26.020009.
- [69] Z. Zhang, S. Liu, J. Peng, M. Yao, G. Zheng, and J. Zhong, "Simultaneous spatial, spectral, and 3D compressive imaging via efficient Fourier single-pixel measurements," *Optica*, vol. 5, no. 3, pp. 315-319, 2018/03/20 2018, doi: 10.1364/OPTICA.5.000315.
- [70] P. Thibault, M. Dierolf, A. Menzel, O. Bunk, C. David, and F. Pfeiffer, "High-resolution scanning x-ray diffraction microscopy," *Science (New York, N.Y.)*, vol. 321, no. 5887, p. 379, 2008, doi: 10.1126/science.1158573.
- [71] G. Scarcelli, V. Berardi, and Y. Shih, "Can two-photon correlation of chaotic light be considered as correlation of intensity fluctuations?," *Physical review letters*, vol. 96, no. 6, p. 063602, 2006, doi: 10.1103/PhysRevLett.96.063602.
- [72] C. Zhao *et al.*, "Ghost imaging lidar via sparsity constraints," *Applied Physics Letters*, vol. 101, no. 14, 2012, doi: 10.1063/1.4757874.
- [73] W. Gong, C. Zhao, H. Yu, M. Chen, W. Xu, and S. Han, "Three-dimensional ghost imaging lidar via sparsity constraint," *Sci Rep*, vol. 6, no. 1, pp. 26133-26133, 2016, doi: 10.1038/srep26133.
- [74] J. H. Shapiro, "Computational ghost imaging," *Physical Review A*, vol. 78, no. 6, p. 061802, 12/18/2008, doi: 10.1103/PhysRevA.78.061802.
- [75] E. Salvador-Balaguer, P. Latorre-Carmona, C. Chabert, F. Pla, J. Lancis, and E. Tajahuerce, "Low-cost single-pixel 3D imaging by using an LED array," *Optics express*, vol. 26, no. 12, p. 15623, 2018, doi: 10.1364/OE.26.015623.

- [76] Z.-H. Xu, W. Chen, J. Penuelas, M. Padgett, and M.-J. Sun, "1000 fps computational ghost imaging using LED-based structured illumination," *Optics express*, vol. 26, no. 3, p. 2427, 2018, doi: 10.1364/OE.26.002427.
- [77] N. Radwell, K. J. Mitchell, G. M. Gibson, M. P. Edgar, R. Bowman, and M. J. Padgett, "Single-pixel infrared and visible microscope," *Optica*, vol. 1, no. 5, p. 285, 2014, doi: 10.1364/OPTICA.1.000285.
- [78] P. E. Matthew *et al.*, "Simultaneous real-time visible and infrared video with single-pixel detectors," *Scientific Reports*, vol. 5, no. 1, 2015, doi: 10.1038/srep10669.
- [79] K. Komatsu, Y. Ozeki, Y. Nakano, and T. Tanemura, "Ghost imaging using integrated optical phased array," ed, 2017, pp. 1-3.
- [80] L. Li-Jing, C. Wen, Z. Xin-Yu, and S. Ming-Jie, "Fast Optical Phased Array Calibration Technique for Random Phase Modulation LiDAR," *IEEE Photonics Journal*, vol. 11, no. 1, pp. 1-10, 2019, doi: 10.1109/JPHOT.2018.2889313.
- [81] D. Phillips *et al.*, "Adaptive foveated single-pixel imaging with dynamic super-sampling," *arXiv.org*, 2016.
- [82] Q. Chen, S. K. Chamoli, P. Yin, X. Wang, and X. Xu, "Imaging of hidden object using passive mode single pixel imaging with compressive sensing," *Laser Physics Letters*, vol. 15, no. 12, p. 126201, 2018/10/23 2018, doi: 10.1088/1612-202x/aae216.
- [83] H. Wu, M. Zhao, F. Li, Z. Tian, and M. Zhao, "Underwater polarization - based single pixel imaging," *Journal of the Society for Information Display*, vol. 28, no. 2, pp. 157-163, 2020, doi: 10.1002/jsid.838.
- [84] R. M. Dickson, D. J. Norris, Y. L. Tzeng, and W. E. Moerner, "Three-dimensional imaging of single molecules solvated in pores of poly(acrylamide) gels," *Science (New York, N.Y.)*, vol. 274, no. 5289, p. 966, 1996, doi: 10.1126/science.274.5289.966.
- [85] T. Bosch, "Laser ranging: a critical review of usual techniques for distance measurement," *Optical Engineering*, vol. 40, no. 1, p. 10, 2001, doi: 10.1117/1.1330700.
- [86] V. Andreas, W. Thomas, G. Otkrist, V. Ashok, G. B. Mounji, and R. Ramesh, "Recovering three-dimensional shape around a corner using ultrafast time-of-flight imaging," *Nature Communications*, vol. 3, no. 1, p. 745, 2012, doi: 10.1038/ncomms1747.
- [87] Y. Zhang, M. P. Edgar, B. Sun, N. Radwell, G. M. Gibson, and M. J. Padgett, "3d single-pixel video," *Journal of Optics*, vol. 18, no. 3, p. 035203, 2016, doi: 10.1088/2040-8978/18/3/035203.
- [88] Q. Guo, H. Chen, Z. Weng, M. Chen, S. Yang, and S. Xie, "Fast time-lens-based line-scan single-pixel camera with multi-wavelength source," *Biomedical optics express*, vol. 6, no. 9, p. 3610, 2015, doi: 10.1364/BOE.6.003610.
- [89] C. Lei, B. Guo, Z. Cheng, and K. Goda, "Optical time-stretch imaging: Principles and applications," *Applied Physics Reviews*, vol. 3, no. 1, 2016, doi: 10.1063/1.4941050.
- [90] Q. Guo, Y.-x. Wang, H.-w. Chen, M.-h. Chen, S.-g. Yang, and S.-z. Xie, "Principles and applications of high-speed single-pixel imaging technology," *Frontiers of Information Technology & Electronic Engineering*, vol. 18, no. 9, pp. 1261-1267, 2017/09/01 2017, doi: 10.1631/FITEE.1601719.
- [91] P. F. McManamon, "Review of ladar: a historic, yet emerging, sensor technology with rich phenomenology," *Optical Engineering*, vol. 51, no. 6, 2012, doi: 10.1117/1.OE.51.6.060901.
- [92] O. Korotkova, "Optical Beam Propagation through the Oceanic Turbulence," in *Frontiers in Optics 2011/Laser Science XXVII*, San Jose, California, 2011/10/16 2011: Optical Society of America, in OSA Technical Digest, p. FWK1, doi: 10.1364/FIO.2011.FWK1. [Online]. Available: <http://www.osapublishing.org/abstract.cfm?URI=FiO-2011-FWK1>
- [93] X. Zhang, L. Hu, and M.-X. He, "Scattering by pure seawater: Effect of salinity," *Optics Express*, vol. 17, no. 7, pp. 5698-5710, 2009/03/30 2009, doi: 10.1364/OE.17.005698.
- [94] S. S. Chen, D. L. Donoho, and M. A. Saunders, "Atomic Decomposition by Basis Pursuit," *SIAM Review*, vol. 43, no. 1, pp. 129-159, 2001, doi: 10.1137/S003614450037906X.

- [95] E. J. Candes and T. Tao, "Near-Optimal Signal Recovery From Random Projections: Universal Encoding Strategies?," *IEEE Transactions on Information Theory*, vol. 52, no. 12, pp. 5406-5425, 2006, doi: 10.1109/TIT.2006.885507.
- [96] E. Candès and J. Romberg, "Sparsity and incoherence in compressive sampling," *Inverse Problems*, vol. 23, no. 3, pp. 969-985, 2007, doi: 10.1088/0266-5611/23/3/008.
- [97] M. Rani, S. B. Dhok, and R. B. Deshmukh, "A Systematic Review of Compressive Sensing: Concepts, Implementations and Applications," *IEEE Access*, vol. 6, pp. 4875-4894, 2018, doi: 10.1109/ACCESS.2018.2793851.
- [98] B. Zhang, Y. Liu, J. Zhuang, K. Wang, and Y. Cao, "Matrix permutation meets block compressed sensing," *Journal of visual communication and image representation*, vol. 60, pp. 69-78, 2019, doi: 10.1016/j.jvcir.2019.02.023.
- [99] Y. Cao, W. Gong, B. Zhang, F. Zeng, and S. Bai, "Optimal Permutation Based Block Compressed Sensing for Image Compression Applications," *IEICE transactions on information and systems*, vol. E101.D, no. 1, pp. 215-224, 2018, doi: 10.1587/transinf.2017EDP7087.
- [100] L. S. Dolin, "Theory of lidar method for measurement of the modulation transfer function of water layers," *Appl Opt*, vol. 52, no. 2, pp. 199-207, 2013, doi: 10.1364/AO.52.000199.
- [101] S. Zhou, S. K. Zhou, H. Greenspan, and D. Shen, Eds. *Deep learning for medical image analysis*, First edition. ed. London, England : Academic Press, 2017.
- [102] L. Lu, L. Lu, Ed. *Deep learning and convolutional neural networks for medical imaging and clinical informatics*, 1st ed. 2019. ed. Cham, Switzerland : Springer, 2019.
- [103] F. Liu, H. Jang, R. Kijowski, T. Bradshaw, and A. B. McMillan, "Deep Learning MR Imaging-based Attenuation Correction for PET/MR Imaging," *Radiology*, vol. 286, no. 2, pp. 676-684, 2018, doi: 10.1148/radiol.2017170700.
- [104] W. W. Labaki and M. K. Han, "Artificial Intelligence and Chest Imaging. Will Deep Learning Make Us Smarter?," *Am J Respir Crit Care Med*, vol. 197, no. 2, pp. 148-150, 2018, doi: 10.1164/rccm.201709-1879ED.